

Absorption, Photoluminescence and Resonant Rayleigh Scattering Probes of Condensed Microcavity Polaritons

F. M. Marchetti,¹ J. Keeling,² M. H. Szymańska,³ and P. B. Littlewood¹

¹*Cavendish Laboratory, University of Cambridge, Madingley Road, Cambridge CB3 0HE, UK*^{*}

²*Department of Physics, Massachusetts Institute of Technology, 77 Mass. Ave., Cambridge, MA 02139, USA*[†]

³*Clarendon Laboratory, Department of Physics, University of Oxford, Parks Road, Oxford, OX1 3PU, UK*

(Dated: Jan 13, 2006)

We investigate and compare different optical probes of a condensed state of microcavity polaritons in expected experimental conditions of non-resonant pumping. We show that the energy- and momentum-resolved resonant Rayleigh signal provide a distinctive probe of condensation as compared to, e.g., photoluminescence emission. In particular, the presence of a collective sound mode both above and below the chemical potential can be observed, as well as features directly related to the density of states of particle-hole like excitations. Both resonant Rayleigh response and the absorption and photoluminescence, are affected by the presence of quantum well disorder, which introduces a distribution of oscillator strengths between quantum well excitons at a given energy and cavity photons at a given momentum. As we show, this distribution makes it important that in the condensed regime, scattering by disorder is taken into account to all orders. We show that, in the low density linear limit, this approach correctly describes inhomogeneous broadening of polaritons. In addition, in this limit, we extract a linear blue-shift of the lower polariton versus density, with a coefficient determined by temperature and by a characteristic disorder length.

PACS numbers: 71.36.+c, 78.35.+c, 78.40.Pg, 71.45.-d

I. INTRODUCTION

Since the prediction of Keldysh and Kopaev,¹ there has been a long and intense pursuit to realise a condensed phase in solid state excitonic, and related, systems. In particular, polaritons in semiconductor microcavities, the coupled eigenstates of an exciton with a cavity photon,^{2,3} represent ideal candidates for observing condensation phenomena. The very light mass of these composite bosonic particles promises relatively high transition temperatures. In the past decade, improvements in the growth technology of semiconductor heterostructures have made the study of high-quality strongly-coupled planar microcavities almost routine for III-V and II-VI semiconductors. The high degree of external control of these systems, and the possibility of direct detection for them has opened the route towards a new generation of fast optical matter-wave lasers and amplifiers.^{4,5,6,7,8} More recently, concerted experimental efforts have been devoted to the realisation of a Bose-Einstein condensate of microcavity polaritons.^{4,9,10,11,12,13,14}

On the experimental side, a challenge to the realisation of a condensed polariton phase might be represented by the finite quality of the cavity mirrors and the resultant short polariton lifetime, of the order of picoseconds. In addition, due to the ‘bottleneck effect’,¹⁵ the relaxation of polaritons to the zero momentum state can be delayed, hindering the creation of a thermal population in the lowest energy state. It has however been recently shown^{13,14,16} that thermalization processes due to particle-particle scattering can be dramatically magnified by increasing the value of the (non-resonant) pump power, and by positively detuning the cavity energy above the excitonic energy. Under these conditions,

the progress towards a zero momentum quasi-equilibrium condensate has been significant,^{4,5,9,10,11,12,13} including a non-linear threshold behaviour in the emission intensity at zero momentum,^{4,5,9,13} the investigation of the second order coherence function,⁹ a characteristic change in the momentum space distribution above threshold,^{10,13} and evidence that the equilibration time is shorter than the polariton lifetime has been seen.¹³ Finally, very recently, a clear demonstration of condensation of cavity polaritons has been demonstrated in CdTe.¹⁴ Kasprzak and collaborators have shown that condensation of equilibrated polaritons can be achieved for effective temperatures around 20K and evidence for condensation has been seen in the occupation function, the first order coherence (both in time and in space) and in the spontaneous appearance of linear polarisation of the condensate emission.

Alongside the experimental effort, a significant theoretical effort has been invested in analysing properties and predicting signatures of polariton condensation.^{17,18,19,20,21,22,23,24,25,26,27,28,29} Much of this work focuses on modelling the conditions under which condensation can occur, both in equilibrium,^{17,20,21,22} and considering the effects of pumping and decay.^{23,26,28,29} Possible signatures include the nonlinear relation of emission at zero momentum to pumping power,^{27,28,29} changes to the linewidth,^{26,27,29} the PL spectrum and the angular distribution of radiation,^{21,22} and spontaneous polarisation of emitted radiation.²⁴

In this paper, we discuss the optical properties of condensed polaritons, focusing our interests on absorption, photoluminescence (PL) and resonant Rayleigh scattering (RRS). From our study we conclude that RRS, the coherent scattering by disorder of polaritons into direc-

tions other than that of the original probe, represents a powerful tool for investigating the condensed phase. We will show that signatures of condensation are visible in the RRS spectrum, allowing a direct probe of the collective excitation properties of the polariton condensate. In particular, we will show that, above the threshold for condensation, strong emission from the collective sound mode both above and below the chemical potential can be seen in the RRS spectra (see Fig. 1). In contrast such features are expected to be much harder to observe in usual PL emission spectra, where the spectrum is dominated by the very strong condensate emission at the chemical potential, which is likely to mask these more subtle features. In addition, we will show that the RRS spectra directly reflects the disorder averaged density of states of excitonic particle-hole like excitations, i.e. bound excitons coupled to the coherent photon field.

Resonant Rayleigh scattering depends on disorder to scatter polaritons between momentum states. In order to carry on our analysis, we introduce a realistic description of disorder and analyse its effects on RRS and more generally on other optical probes, like absorption and PL. To do this, we make use of a quantitatively accurate model for exciton disorder,^{30,31,32} and numerically evaluate the distribution of excitonic energies and oscillator strengths associated with a given disorder potential. An accurate treatment of exciton disorder for quantum wells in microcavities is important because the large ratio of exciton mass to photon mass means that those exciton states contributing most to the thermally populated polaritons are strongly localised, i.e. cannot be treated within the first Born approximation. Such a treatment shows that, for a given exciton energy and momentum, there is still a distribution of possible oscillator strengths. For the exciton states relevant to polariton formation, the distribution of oscillator strengths varies from a narrow Gaussian at low energies (below the band edge) to a Porter-Thomas distribution at high energies, as is known from previous works.^{30,31,32} Here, we study the effect of this distribution on the many-body physics, and in particular, on RRS and PL spectra.

In this paper, we consider the case relevant to the existing CdTe or GaAs microcavities of high-quality quantum wells, where the typical excitonic disorder amplitude is smaller than the Rabi splitting. In this regime, we can make use of the *coupled oscillator model* or wave vector conserving approximation, as explained in Ref. 33. As will be explained in more detail later on, this corresponds to approximating the full exciton Green's function by its momentum-diagonal part (or equivalently considering its disorder average), and treating perturbatively the off-diagonal terms. In this way, the translational invariance broken by the presence of the disorder is restored, polaritons have a defined wave vector and, at high enough densities, condense in the lowest momentum state. Such a treatment implies that excitonic disorder, being on short length scales, does not lead to spatial inhomogeneity on the length scale associated with the polariton. Extended

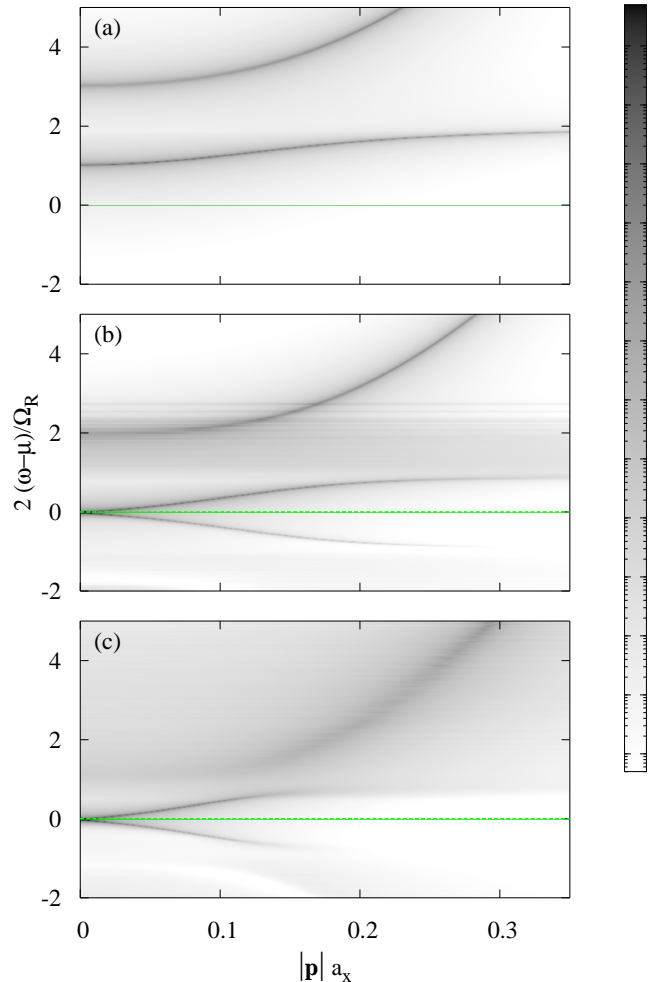


FIG. 1: (Color online) Contourplot of the disorder averaged RRS intensity $\langle I_{pq}(\omega) \rangle$ for $|\mathbf{p}| = |\mathbf{q}|$ as a function of the dimensionless momentum $|\mathbf{p}|a_x$ and rescaled energy $2(\omega - \mu)/\Omega_R$, for zero detuning, Rabi splitting $\Omega_R = 26$ meV, temperature $k_B T = 20$ K, and a disorder strength characterize by an inverse scattering time $1/\tau = 1.16$ meV. (a) non-condensed regime ($\rho \simeq 0$); (b) condensed regime ($\rho \simeq 7.8 \times 10^{-3}$); (c) condensed regime ($\rho \simeq 6.7 \times 10^{-2}$). (The parameters chosen for these plots are the same as those used later for spectral weight and photoluminescence.) The value of the chemical potential is explicitly marked [horizontal green (gray) line]. While in the non-condensed regime, RRS emission is always above the chemical potential, in the condensed phase, emission from the collective sound mode is seen both above and below the chemical potential.

polaritons are formed from a superposition of many localised excitons, therefore recovering translational invariance at the level of polaritons. At low densities, in the non-condensed state, many observable properties can be adequately described by the coupled oscillator model and so can be found from the mean squared oscillator strength at a given energy. In this limit our method recovers the

well known results for the inhomogeneous broadening of the polariton PL,^{33,34} and — by considering in addition the mean fourth power of the oscillator strength — the averaged RRS response.^{35,36,37,38} However, when condensed, there are observable effects associated with the full distribution of oscillator strengths. In particular, the non-vanishing probability of excitons to have arbitrarily small oscillator strengths has direct consequences for optical probes, including both RRS and PL.

In Ref. 25, we considered specific aspects of resonant Rayleigh scattering arising from the model discussed in this paper. Here, we provide and compare further experimental probes of condensation, and discuss the underlying physical mechanisms involved. All these optical probes, including RRS, are in addition to a non-resonant pumping of the microcavity polaritons. A related problem is studied in Ref. 39. There, the Rayleigh scattering of a strong resonant pump is considered (treating disorder perturbatively), thus the probe is the pump. In this paper, in contrast, one has to distinguish two types of coherence. The first type is the internal coherence of the condensed system, which arises spontaneously following non-resonant pumping. The second type is the coherent scattering of an external laser probe on disorder, which can be strongly modified by the presence of the condensate.

The form of the density of states, optical density, and distribution of oscillator strengths found from the numerical calculations are also important in other thermodynamic properties and probes of polaritons. One such example is the calculation of the linear blue-shift vs. density in the low density regime. The inclusion of exciton states that couple weakly to photons extends the validity of the current model to densities beyond those in similar treatments,^{17,21} and provides a stronger basis for the use of those models in the regimes where they are valid.

The paper is arranged in the following sections: We describe the effect of quantum well disorder on the exciton oscillator strength in Sec. II. There, we also give details of the numerical analysis (Sec. II A), which will be used in the many-body model introduced in Sec. III to describe the thermodynamics of polariton condensation (Sec. III A). Section IV describes the optical probes such as spectral weight and photoluminescence (Sec. IV A) and resonant Rayleigh scattering (Sec. IV C). Conclusions are collected in Sec. V, while Appendix A explains how one can detect RRS using phase sensitive measurements.

II. EXCITONS IN DISORDERED QUANTUM WELLS

The problem of an exciton in a disordered quantum well has been studied at some length in the last two decades.^{30,31,32,40,41,42,43} Quantum well disorder can arise due to interface and alloy fluctuations and affects the properties of the excitonic linewidth and absorption spec-

trum. Similarly to Refs. 30,31, we will assume the external disorder potential to be correlated on a length scale larger than the exciton Bohr radius. Accordingly, we factorise the excitonic in-plane relative and centre of mass coordinates

$$\Psi_\alpha(\mathbf{r}_e, \mathbf{r}_h) \simeq \varphi_{1s}(r) \Phi_\alpha(\mathbf{R})$$

$$\varphi_{1s}(r) = \sqrt{8/\pi a_x^2} e^{-2r/a_x},$$

and assume that the disorder affects only the excitonic centre of mass motion $\Phi_\alpha(\mathbf{R})$, while the internal degrees of freedom can be restricted to the ground state hydrogenic state $\varphi_{1s}(r)$. Here, $a_x = \epsilon/e^2 \mu_r$ is the exciton Bohr radius and μ_r the reduced mass (henceforth we will set $\hbar = 1$). Neglecting the transverse degrees of freedom related to the confinement of the excitons in the QW, the energy associated to the wavefunction $\Psi_\alpha(\mathbf{r}_e, \mathbf{r}_h)$ is given by the sum of the relative motion energy E_x [i.e., the band gap minus the exciton binding energy, $\mathcal{R}_{yx} = (2\mu_r a_x^2)^{-1} = e^4 \mu_r / 2\epsilon^2$] and the energy related to the centre of mass motion ε_α :

$$\left[-\frac{\nabla_{\mathbf{R}}^2}{2m_x} + V(\mathbf{R}) + E_x \right] \Phi_\alpha(\mathbf{R}) = \varepsilon_\alpha \Phi_\alpha(\mathbf{R}). \quad (1)$$

Here, the effective disorder potential $V(\mathbf{R})$ represents the microscopic structural disorder averaged over the electron-hole motion.³⁰ This can be approximated, e.g., with a Gaussian noise correlated on a length scale $\ell_c > a_x$ with variance equal to σ^2 :

$$\langle V(\mathbf{R})V(\mathbf{R}') \rangle = (\sigma^2 \ell_c^2 / L^2) \sum_{\mathbf{q}} e^{i\mathbf{q} \cdot (\mathbf{R} - \mathbf{R}')},$$

where L^2 is the quantisation area. It will be convenient, later on, to introduce the scattering time

$$\tau = \frac{1}{2\pi\nu\sigma^2\ell_c^2},$$

where $\nu = m_x/2\pi$ is the two-dimensional density of states in the clean limit.

In two dimensional non-interacting systems, all states are localised by the disorder potential. However, the localisation length and the character of the excitonic wavefunction change significantly from below to above the band edge E_x . Well below the band edge, low-energy Lifshitz tail states,⁴⁴ are well localised in deep potential minima, with a nodeless (roughly Gaussian) shape. These states are rare, because they occur due to large, rare, fluctuations of the disorder potential. In contrast, higher energy states above the band edge have a fractal-like shape with many nodes and can be approximated by a random superposition of plane waves with the same momentum $|\mathbf{p}| \simeq \sqrt{2m_x(\varepsilon_\alpha - E_x)}$. Here, the localisation mechanism is closely related to quantum mechanical interference effects.

Accordingly, the change of the shape of the centre of mass wavefunctions across the band edge is accompanied by a dramatic change in the excitonic oscillator

strength.³¹ The oscillator strength describing coupling of a quantum well exciton to light, $g_{\alpha,\mathbf{p}}$, is given by the probability amplitude of finding an electron and a hole at the same position and with centre of mass momentum equal to the photon momentum \mathbf{p} and is therefore proportional to the Fourier transform of the centre of mass wave function, $\Phi_{\alpha,\mathbf{p}} = \langle \Phi_{\alpha} | \mathbf{p} \rangle$:

$$g_{\alpha,\mathbf{p}} = e d_{ab} \sqrt{\frac{2\pi\omega_{\mathbf{p}}}{\epsilon L_w}} \varphi_{1s}(0) \Phi_{\alpha,\mathbf{p}}, \quad (2)$$

where, d_{ab} is the dipole matrix element. The dispersion for photons in a microcavity of width L_w is given by $\omega_{\mathbf{p}} = \sqrt{\omega_0^2 + (c\mathbf{p})^2/\epsilon}$, where $\omega_0 = 2\pi c/L_w \sqrt{\epsilon}$, and can be approximated, for small momenta, by a parabolic dispersion $\omega_{\mathbf{p}} \simeq \omega_0 + \mathbf{p}^2/2m_{ph}$, with the photon mass given by $m_{ph} = 2\pi\sqrt{\epsilon}/cL_w$.

Because there may be many different exciton wavefunctions corresponding to similar exciton energies, the oscillator strength $g_{\alpha,\mathbf{p}}$ is a random quantity, which varies both in phase and magnitude. Considering many disorder realisations, we find a distribution of squared oscillator strengths, $|g_{\alpha,\mathbf{p}}|^2$ as a function of the energy ε_{α} and momentum \mathbf{p} . This distribution reflects the statistical properties of the centre of mass excitonic wave functions.

To compare to experimentally relevant observables, we introduce the density of states (DoS),

$$\text{DoS}(\varepsilon) \equiv \frac{1}{L^2} \sum_{\alpha} \langle \delta(\varepsilon - \varepsilon_{\alpha}) \rangle,$$

and the mean squared oscillator strength:

$$g^2(\varepsilon, |\mathbf{p}|) = \frac{1}{\text{DoS}(\varepsilon)} \langle \sum_{\alpha} |g_{\alpha,\mathbf{p}}|^2 \delta(\varepsilon - \varepsilon_{\alpha}) \rangle, \quad (3)$$

where $\langle \dots \rangle$ is the average over different disorder realisations. These quantities are related to the excitonic optical density by the relation:

$$D(\varepsilon) = \text{DoS}(\varepsilon) g^2(\varepsilon, 0). \quad (4)$$

Experimentally, the excitonic optical density can be measured by dividing the PL emission by the excitonic occupation.³⁴

Focusing for the moment on average properties, rather than on the entire distribution, a simple expression exists for the mean squared oscillator strength in the high energy limit. In this limit, where the DoS is flat and energy independent, $\text{DoS}(\varepsilon) \simeq \nu$, making use of the Born approximation, the squared average oscillator strength $g^2(\varepsilon, |\mathbf{p}|)$ does not depend separately on the disorder potential correlation length ℓ_c and variance σ , but instead only on the scattering time τ (see Fig. 2):

$$g^2(\varepsilon, |\mathbf{p}|) \simeq \frac{1}{m_x \tau L^2} \frac{1}{(\varepsilon - \varepsilon_{\mathbf{p}})^2 + (1/2\tau)^2}, \quad (5)$$

where $\varepsilon_{\mathbf{p}} = E_x + \mathbf{p}^2/2m_x$ is the free particle dispersion. From this form, and the effectively constant density of

states, one can see that both the mean squared oscillator strength and the excitonic optical density are symmetrical. The comparison of this approximate form to the numerical simulation is shown in Fig. 2,

In contrast, for energies much below the band edge, the specific asymptotic expression of $g^2(\varepsilon, |\mathbf{p}|)$ depends whether the correlation length ℓ_c is smaller or larger than the localisation length $r_{\Phi}(\varepsilon)$. In the white noise limit,⁴⁴ $\ell_c \ll r_{\Phi}(\varepsilon) \sim (2m_x|\varepsilon - E_x|)^{-1/2}$, one can show that the centre of mass wavefunction $\Phi_{\alpha}(\mathbf{R})$ can be approximated by a Gaussian centred at a randomly distributed site \mathbf{R}_{α} ,

$$\Phi_{\alpha}(\mathbf{R}) = r_{\Phi}^{-1} e^{-(\mathbf{R} - \mathbf{R}_{\alpha})^2/r_{\Phi}^2}$$

$$\Phi_{\alpha,\mathbf{p}} = r_{\Phi} e^{i\mathbf{p} \cdot \mathbf{R}_{\alpha} - (r_{\Phi}\mathbf{p})^2/4},$$

and therefore giving a squared oscillator strength proportional to:

$$|\Phi_{\alpha,\mathbf{p}}|^2 \simeq \frac{1}{2m_x|\varepsilon - E_x|} e^{-|\mathbf{p}|^2/(4m_x|\varepsilon - E_x|)}.$$

Thus, here the distribution of squared oscillator strengths is very narrow, with a mean square value given by the above form.

Similarly, much theoretical (and numerical) work has been done to establish the energy dependence of the density of states. In the low energy tail, as before, the specific asymptotic form of the DoS depends on the value of the correlation length ℓ_c . In the white noise limit, one can show that $\text{DoS}(\varepsilon) \propto |\varepsilon - E_x|^{3/2} e^{-11.8|\varepsilon - E_x|/\sigma^2 m_x \ell_c^2}$, while, in the opposite (classical) limit, $\ell_c \gg r'_{\Phi}(\varepsilon) \sim (2\ell_c/\sqrt{2m_x|\varepsilon - E_x|})^{1/2}$, instead one has $\text{DoS}(\varepsilon) \propto (\varepsilon - E_x)^2 e^{-(\varepsilon - E_x)^2/2\sigma^2}$ (see, e.g., Ref. 42). In general, for the finite values of the disorder correlation length corresponding to typical experiments, the regions in energy where one of these two analytical regimes apply are very restricted, and therefore a numerical analysis is required.

Numerical analysis is also essential in order to account for the distribution of squared oscillator strengths $|g_{\alpha,\mathbf{p}}|^2$ near the band edge. This distribution changes substantially from low energy states to high energy ones. As we discuss more in detail in the next section, for high energy states the oscillator strength distribution is governed by a Porter-Thomas law, while for Lifshitz tail states the distribution follows a narrow Gaussian-like distribution. Neither of these distributions apply for energies around the band edge. However, it is states near the band edge that have the largest optical density, and so the distribution of oscillator strengths in this region has a significant impact on derived quantities. It thus becomes essential to use numerical analysis to find the entire distribution of oscillator strengths.

A. Numerical Analysis

To solve Eq. (1), we exactly diagonalise this problem within a finite basis set, using conjugate-gradient minimisation with pre-conditioning of the steepest descent

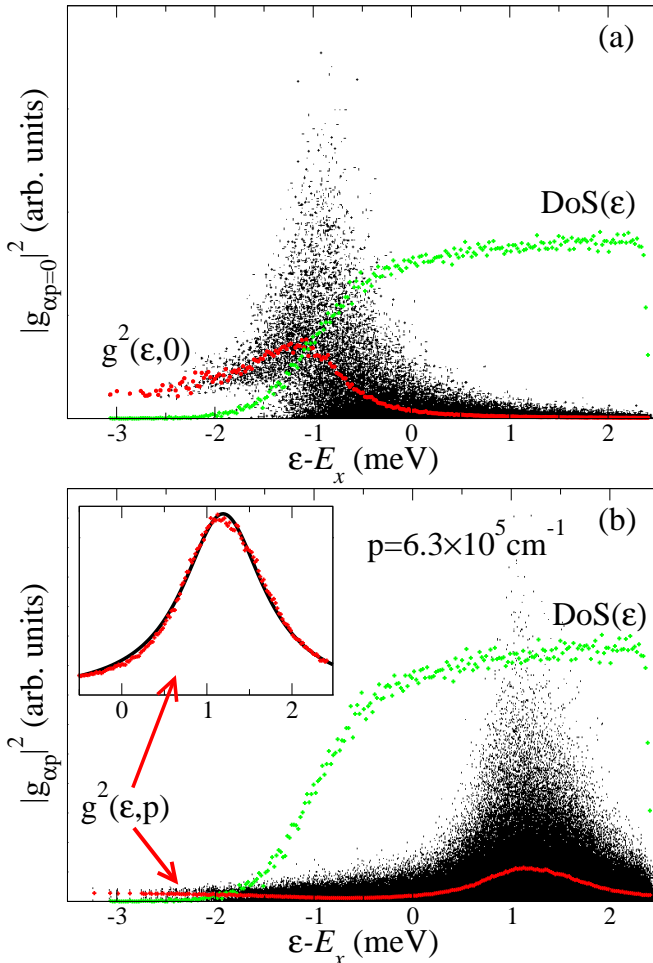


FIG. 2: (Color online) Plot showing the energy dependence of the excitonic squared coupling strength $|g_{\alpha,p}|^2$ to photons of momentum $|\mathbf{p}| = 0$ (a) (from Ref. 25, for comparison) and $|\mathbf{p}| = 6.3 \times 10^5 \text{ cm}^{-1}$ (b), where all exciton states found numerically. Results are taken from 160 different realizations of disorder potential, and for (b), coupling strengths from eight different photon momenta (p_x, p_y) with the same value of $|\mathbf{p}|$ are combined. The mean squared averaged oscillator strength $g^2(\epsilon, |\mathbf{p}|)$ for the same value of momentum [lower red (gray) points] and the density of states $\text{DoS}(\epsilon)$ [upper green (gray) points] are also explicitly plotted. Inset: Fit of $g^2(\epsilon, |\mathbf{p}|)$ to the expression (5) with a renormalized energy ϵ_p .

wavevector (for a detailed discussion of this method, see Ref. 45). We find the exact eigenvalues and eigenfunctions in a finite basis on a grid of 120×120 points for a system of size $L = 1\mu\text{m}$, $\sigma = 2\text{meV}$, $\ell_c = 166\text{\AA}$ and excitonic mass $m_x/m_0 = 0.08$. These parameters give an inverse scattering time of $1/\tau = 1.16\text{meV}$. For this choice of the grid, one can show that convergence is reached. From the evaluated eigenvalues ϵ_α and eigenstates $\Phi_{\alpha,p}$ over 160 realisations of the disorder potential, we can derive the excitonic density of states, the oscillator coupling strength and its squared average, Eq. (3), which we plot in Figs. 2, and 3, while the corresponding optical density

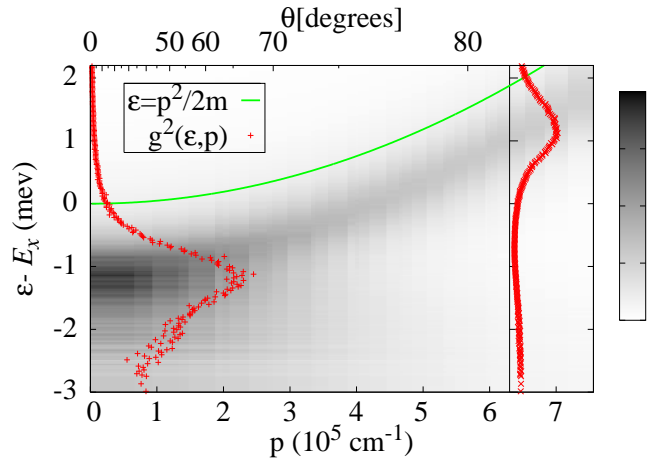


FIG. 3: (Color online) Contourplot of the mean (over 160 realizations of the disorder potential) squared oscillator strength $g^2(\epsilon, |\mathbf{p}|)$ versus energy and momentum [or equivalently angle $\theta = \tan^{-1}(c|\mathbf{p}|/\omega_0)$]. Note that the scale in angle is not linear. The free particle dispersion $E_x + |\mathbf{p}|^2/2m_x$ [solid green (gray) line], and the a trace of the mean squared oscillator strength for two representative values of momenta, $|\mathbf{p}| = 0$ ($\theta = 0^\circ$) and $|\mathbf{p}| = 6.3 \times 10^5 \text{ cm}^{-1}$ ($\theta = 82^\circ$) [red (gray) plus symbols] are explicitly plotted (cf Fig. 2). The figure is adapted from Ref. 25.

is plotted in Fig. 4.

The lower panel of Fig. 2 shows the squared coupling strength $|g_{\alpha,p}|^2$ versus energy for a fixed value of momentum, $|\mathbf{p}| = 6.3 \times 10^5 \text{ cm}^{-1}$, corresponding, for a cavity of $\omega_0 = 1.68\text{eV}$, to an angle of $\theta = \tan^{-1}(c|\mathbf{p}|/\omega_0) = 82^\circ$. Note that, because of the presence of disorder in the quantum well, one photon with a given momentum couples with many exciton states with different energies. We will see later on therefore that a polariton with a given momentum is formed by the superposition of one photon state $|\mathbf{p}\rangle$ and many exciton states $|\Phi_\alpha\rangle$. These states are more or less strongly coupled depending on the distribution of oscillator strength for that given momentum. As Fig. 2 shows, by probing a quantum well at a large angle, i.e. with high momenta photons, the excited excitons with larger oscillator strength are the ones which are almost-delocalised in nature and with a many-node fractal-like shape. By taking the average over many (160) disorder realisations, the squared average oscillator strength $g^2(\epsilon, |\mathbf{p}|)$ shown in the inset in Fig. 2 is well described by the Lorentzian shape predicted by the Born approximation of Eq. (5), with a fitted width of $1/\tau_{\text{fit}} \simeq 1.2\text{meV}$ in good agreement with the theoretical value $1/\tau = 1.16\text{meV}$. However, the peak of the Lorentzian does not coincide with the energy of the clean limit, ϵ_p , but is renormalised down in value, as can be shown by employing a self-consistent Born approximation.

In contrast, as shown in the upper panel of Fig. 2, for photons with zero momentum, the maximum value of

the oscillator strength characterises excitonic states below the band edge which are more localised in nature. This can be easily understood by the following qualitative argument: At very low energies, the excitonic state is strongly localised in a deep potential minimum and has no nodes. Increasing the energy, at first the localisation length increases [e.g., $r_\Phi(\varepsilon) \sim (2m_x|\varepsilon - E_x|)^{-1/2}$ in the white noise limit] and thus increases the oscillator strength. However, eventually, the wavefunction starts developing nodes and consequently the squared average oscillator strength decreases. When $\mathbf{p} = 0$, only the high energy side of $g^2(\varepsilon, 0)$ can be described by the Born limit (5). For the chosen values of the disorder potential correlation length ℓ_c and variance σ , an analytical expression for the low energy (Lifshitz) tail is not known.

The crossover from localised to more plane-wave-like excitonic states obtained by increasing the value of the photon momentum is plotted in Fig. 3. At high momenta, the maximum of the squared average oscillator strength $g^2(\varepsilon, |\mathbf{p}|)$ shown in Fig. 3 follows the free particle dispersion, plus a renormalisation down in energy, which decreases for higher photon momenta, i.e. these states are described well by free particles, including disorder in the first Born approximation. At low momenta, the states which have the stronger oscillator strength are effectively localised. The crossover, as seen in the contour plot, happens at relatively large angle, $\theta \simeq 55^\circ$, because of the large ratio of exciton to photon mass: The crossover momentum is set by exciton mass, but its conversion to an angle depends on effective photon mass. For a connected reason, the thermally populated polariton states are formed out of strongly localised (i.e. beyond first Born approximation) excitonic states: For values of temperature and photon mass relevant for experiments, thermal population of polaritons extends up to around 10° in momentum, which as seen in Fig. 3 corresponds to exciton states not accurately described by the Born approximation. For this reason, in the following we will concentrate on the oscillator strength corresponding to $\mathbf{p} \simeq 0$, $|g_{\alpha,0}|^2$.

Finally we plot in Fig. 4 the optical density. For the chosen values of ℓ_c and σ , the optical density shows a maximum around $\varepsilon^* - E_x \simeq -0.94\text{meV}$ below the band edge, a full width at half maximum (FWHM) of approximatively $\sigma^* \simeq 0.94\text{meV}$ and a clear asymmetry of the line-shape. It is well known^{32,43} that, by indicating with $E_c = 1/2m_x\ell_c^2$ the confinement energy of the lowest state in a typical potential minimum, the excitonic line shape is determined by the ratio E_c/σ and, for a finite value of this, the optical density develops an asymmetry towards higher energies. For our choices of parameters, $E_c/\sigma \simeq 0.85$. Asymmetry of the optical density of quantum well excitons has been also measured experimentally (see, e.g., Ref. 34), by dividing the measured PL by the excitonic occupation.

As mentioned earlier, the full distribution of oscillator strengths, and not just its mean squared value will be important. It is useful to discuss here some technical details

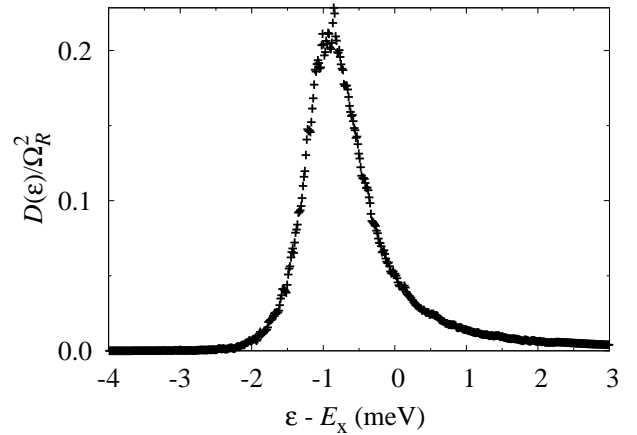


FIG. 4: Optical density Eq. (4) versus energy. The maximum value is around $\varepsilon^* - E_x \simeq -0.94\text{meV}$ and the FWHM $\sigma^* \simeq 0.94\text{meV}$.

of how this is extracted. The numerical analysis provides the excitonic eigenvalues and eigenstates only within a finite interval in energy. (The lowest energy states arise from rare potential fluctuations, which would require a larger region of space to be sampled; the highest energy states have spatial variation on lengthscales finer than our grid.) Within the interval of energies found, averages are performed making use of the raw data coming from 160 realisations of the disorder potential; outside this interval, averages are taken by extrapolating the numerics. In particular, in the low energy Lifshitz tail, as the oscillator strengths have a narrow Gaussian distribution around its squared averaged value, we approximate the distribution of $|g_{\alpha,0}|^2$ with a delta function at its extrapolated value $g^2(\varepsilon, 0)$. In the very high energy region, instead, we make use of the Porter-Thomas distribution,

$$\mathcal{P}(x = |g_{\alpha,0}|^2) = \frac{\exp[-x/(2\bar{x})]}{\sqrt{2\pi\bar{x}\bar{x}}},$$

where $\bar{x} = g^2(\varepsilon, 0)$, again extrapolating the fitted value for the squared averaged oscillator strength. In addition, we fix the overall scale of $|g_{\alpha,0}|^2$ to match integrated optical intensity with half the experimentally measured Rabi splitting Ω_R squared:

$$\int d\varepsilon D(\varepsilon) = \frac{\Omega_R^2}{4} \quad (6)$$

This normalisation accounts for factors other than the wavefunction in Eq. (2).

Having described the effect of quantum well disorder on the energies of excitons and on their dipole coupling to the cavity photons, we will next introduce the many-body Hamiltonian that will allow us to describe a system of thermalized interacting polaritons which, for a given density and temperature, can condense to a superfluid phase.

III. THE POLARITON MODEL

The Hamiltonian describing a model of excitons with random energies ε_α , corresponding to the centre of mass eigenstate from Eq. (1), dipole coupled to a cavity mode can be written as

$$\hat{H} = \sum_\alpha \frac{\varepsilon_\alpha}{2} (b_\alpha^\dagger b_\alpha + a_\alpha a_\alpha^\dagger) + \sum_{\mathbf{p}} \omega_{\mathbf{p}} \psi_{\mathbf{p}}^\dagger \psi_{\mathbf{p}} + \frac{1}{\sqrt{L^2}} \sum_\alpha \sum_{\mathbf{p}} (g_{\alpha, \mathbf{p}} \psi_{\mathbf{p}} b_\alpha^\dagger a_\alpha + \text{h.c.}) . \quad (7)$$

The description of exciton-exciton interaction in this model is somewhat simplified: it imposes the constraint that two excitons cannot occupy the same energy level ε_α , because of their composite fermionic nature. This constraint is implemented by representing each energy level [where energy levels are distributed according to the density of states, $\text{DoS}(\varepsilon)$] by two possible states, respectively $|\text{g.s.}\rangle$ and $|\text{ex.}\rangle$. These two states are then represented by occupation of two fermionic states, so that the ground state $|\text{g.s.}\rangle = a_\alpha^\dagger |0\rangle$, and an excitonic state $|\text{ex.}\rangle = b_\alpha^\dagger |0\rangle = b_\alpha^\dagger a_\alpha |\text{g.s.}\rangle$. Imposing a constraint on total fermion occupancy, $b_\alpha^\dagger b_\alpha + a_\alpha^\dagger a_\alpha = 1$, eliminates the unphysical states $|0\rangle$ and $a_\alpha^\dagger b_\alpha^\dagger |0\rangle$. In this way saturation effects are introduced to all orders. Note that these fermionic operators a_α^\dagger cannot be written as a linear combination of free electron and hole operators – this is a result of having already included the intra-exciton Coulomb interaction.

The transition matrix element between a photon state $\psi_{\mathbf{p}}^\dagger |\text{g.s.}\rangle$ and an exciton state, $\langle \text{ex.}| = \langle \text{g.s.}| a_\alpha^\dagger b_\alpha$, is given by $g_{\alpha, \mathbf{p}}$ from Eq. (2) and evaluated numerically, as explained in the previous section. It is convenient to rescale this coupling according to

$$g_{\alpha, \mathbf{p}} \mapsto g_{\alpha, \mathbf{p}} \sqrt{\mathcal{R}_{yx} m_x / 2\pi} ,$$

where $N = \mathcal{R}_{yx} L^2 m_x / 2\pi$ is the inverse level spacing $L^2 m_x / 2\pi$, measured in units of the excitonic Rydberg energy. This corresponds to measuring the density of particles per Bohr radius squared. Using these units, we may write the total number of excitations

$$\hat{N} = \sum_\alpha \frac{1}{2} (b_\alpha^\dagger b_\alpha + a_\alpha a_\alpha^\dagger) + \sum_{\mathbf{p}} \psi_{\mathbf{p}}^\dagger \psi_{\mathbf{p}} \quad (8)$$

in a dimensionless form by introducing a dimensionless density of particles $\rho \equiv \langle \hat{N} \rangle / N$, or equivalently $\rho = \langle \hat{N} \rangle / L^2 a_x^2 4\pi\mu/m_x$, where $\langle \hat{N} \rangle / L^2$ is the physical areal density of particles.

In the limit of vanishing density, our occupancy constraint has no effect, and so this description is equivalent to one treating excitons as bosons. As will be shown later, in Sec. IV B, for low densities, our occupancy constraint is also equivalent to a model of excitons as bosons, but with some effective saturation interaction.⁶⁰ Thus, as in the bosonic case, saturation effects are linear^{46,47} and

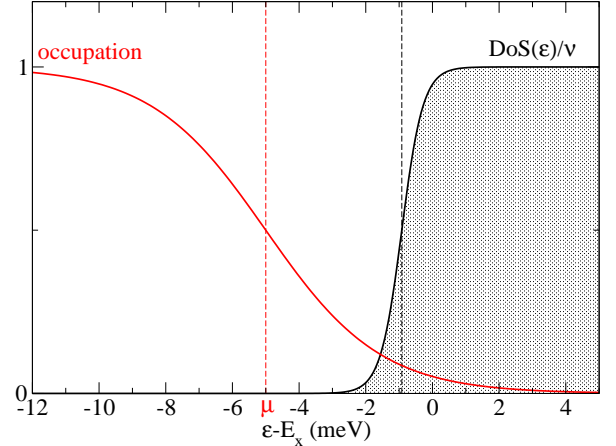


FIG. 5: (Color online) Normalized density of states $\text{DoS}(\varepsilon)/\nu$ and thermal occupation factor [red (gray) line starting at top left] for $E_x - \mu = 5\text{meV}$ and $k_B T = 20\text{K}$.

the blue-shift increases linearly in density. There is however an important difference to those previous works. In contrast to the clean systems studied there, our effective saturation interaction has a coefficient related to disorder and temperature rather than to the Rabi splitting and Bohr radius only. However, increasing the density, saturation effects, and thus the underlying fermionic degrees of freedom become more and more important, and the conventional linear treatment becomes inadequate. In our treatment saturation effects are introduced exactly and taken into account to all orders. Our model is accurate as far as the occupancy is restricted to the strongly localised Lifshitz states in the tail below the band edge (see Fig. 5). All the results described here respect this limit. One can moreover show that it is this density regime which is relevant for on-going experiments in CdTe.¹⁴ Higher energy states, beyond the Lifshitz tail, contribute to the optical response, however they are only weakly occupied, and so the above limit remains valid.

What the model Eq. (7) does not include is the Coulomb interaction between excitons with different energies ε_α , i.e., at low densities, on different localisation sites \mathbf{R}_α . This contribution is expected to be small in the low density regime. This low density regime will be observed all the way through this paper. At the same time we are not including double-occupancy of a single exciton energy level, which could be important at higher densities.

In the following, we will make extensive use of the numerical analysis of oscillator strength distributions explained in the previous section. Let us note here again that in the non-condensed regime, the full distribution is unnecessary – the excitonic optical density is sufficient to derive the polariton dispersion and its inhomogeneous broadening. However, in the condensed phase, and in order to correctly describe resonant Rayleigh scattering mechanisms, we will see that it is of fundamental im-

portance to consider the entire distribution of oscillator strength.

We consider a thermal equilibrium system of polaritons, as describing the situation with non-resonant pumping and strong thermalization processes. This limit has been recently demonstrated to be accessible in ongoing experiments.^{13,14} The total density of polaritons is fixed by introducing a chemical potential μ . Making use of standard path integral techniques and of the grand canonical ensemble, $\hat{H} - \mu\hat{N}$, we integrate over the fermionic fields, and thus write the partition function $\mathcal{Z} = \text{tr}[e^{-\beta(\hat{H}-\mu\hat{N})}]$, with $\beta = 1/k_B T$, in terms of the following imaginary time action:

$$S[\psi] = \int_0^\beta d\tau \sum_{\mathbf{p}} \psi_{\mathbf{p}}^* (\partial_\tau + \tilde{\omega}_{\mathbf{p}}) \psi_{\mathbf{p}} - \text{Tr} \ln G^{-1}. \quad (9)$$

Here, G^{-1} is the, energy level diagonal, inverse single-particle Green's function:

$$G_\alpha^{-1} = \begin{pmatrix} \partial_\tau + \tilde{\varepsilon}_\alpha/2 & \sum_{\mathbf{p}} g_{\alpha,\mathbf{p}} \psi_{\mathbf{p}} / \sqrt{N} \\ \sum_{\mathbf{p}} g_{\alpha,\mathbf{p}}^* \psi_{\mathbf{p}}^* / \sqrt{N} & \partial_\tau - \tilde{\varepsilon}_\alpha/2 \end{pmatrix}, \quad (10)$$

where $\tilde{\varepsilon}_\alpha = \varepsilon_\alpha - \mu$ and $\tilde{\omega}_{\mathbf{p}} = \omega_{\mathbf{p}} - \mu$ are respectively the excitonic and photonic energies measured with respect to the chemical potential. Within this path integral formulation, it is possible to show⁴⁸ that the constraint on the site occupation can be taken into account elegantly by shifting the fermionic Matsubara frequencies according to

$$\epsilon_n = (2n+1)\pi/\beta \mapsto \epsilon_n = (2n+3/2)\pi/\beta,$$

which we will assume from here on in.

A. Mean-Field Phase Diagram

We will see later in section IV how the formation of polaritons, the result of strong coupling between photons and excitons, influences the optical response and in particular how the optical response is affected when the system enters a condensed phase. This section will discuss the mean-field equations, and resultant phase diagram; however first we wish to stress an important point. As observed previously, the relevant polariton states form from the mixing of a photon with a given momentum to many localised excitonic states with different energies. The strength of this mixing is determined by the distribution of oscillator strengths. Although the quantum well excitons may be disorder-localised, for a weak disorder potential, with $\sigma < \Omega_R$, and in the absence of strong photon disorder (which in some cases can also be relevant^{38,49}) the resultant polaritons are delocalised. As such, polaritons will be described by a momentum quantum number, and condense, as in the usual picture, in the lowest momentum state.

The static and uniform minimum $\psi_{\mathbf{p}}(\tau) = \psi\delta_{\mathbf{p},0}$ of the action (9) can be found from the equation of motion, or

saddle-point equation, which has to be solved together with the mean-field equation for the total number of excitations (8):

$$\tilde{\omega}_0 = \frac{1}{N} \sum_{\alpha} |g_{\alpha,0}|^2 \frac{\tanh \beta E_{\alpha}}{2E_{\alpha}} \quad (11)$$

$$\rho = \frac{1}{N} \psi^2 + \frac{1}{N} \sum_{\alpha} \left[\frac{1}{2} - \frac{\tilde{\varepsilon}_{\alpha} \tanh \beta E_{\alpha}}{4E_{\alpha}} \right]. \quad (12)$$

Here, the spectrum of particle-hole excitations, i.e. the quasi-particle spectrum discussed later, is controlled by the energy of an exciton in presence of a coherent photon field ψ , and is given by:

$$E_{\alpha} = \sqrt{(\tilde{\varepsilon}_{\alpha}/2)^2 + |g_{\alpha,0}|^2 \psi^2 / N}. \quad (13)$$

In the following, we will solve simultaneously these coupled equations, both above ($\psi = 0$) and below ($\psi \neq 0$) the critical temperature for condensation. It is interesting to compare these with similar equations which have been already considered, e.g., in the BCS theory of superconductivity,⁵⁰ or in models describing gases of fermionic atoms close to a Feshbach resonance.⁵¹ Considering particularly the case of Feshbach resonance, the density of particles is typically kept fixed, while the interaction strength can be varied externally to span across a BEC condensate of tightly bound fermionic molecules and a BCS state of loosely bound fermionic pairs. In our case, two main important differences arise. Firstly, density is the parameter which is changed. Secondly, the coupling strength of excitons with cavity light depends on the excitonic energy. There is a wide variety of behaviour that can come from these coupled equations (11) and (12), controlled by the distribution of oscillator strengths and by changing the density of states.

By solving the ‘gap equation’ Eq. (11) in the limit $\psi \rightarrow 0$, let us concentrate for the moment on the critical temperature T_c as a function of the chemical potential μ , forgetting about the corresponding excitation density. At the phase boundary, where $\psi = 0$, in contrast to inside the condensed phase, the squared oscillator strength appears only linearly in Eq. (11), this expression therefore involving only the optical density $D(\varepsilon)$. It is clear that the standard BCS result can be thought of as a limiting case where the effective optical density is much wider than the temperature.⁵² In the opposite limit, of a narrow delta-like optical density, one can solve the gap equation analytically.¹⁷

By taking into account the density equation (12), the critical temperature can be expressed as a function of the excitation density rather than as a function of the chemical potential. In the standard BCS theory there is no modulation of the interaction strength and therefore no difference between optical density $D(\varepsilon)$ and density of states DoS(ε). In our system instead one has to introduce separately both quantities, and further a realistic description of the DoS is required in order to measure the density in physical units. In previous treatments,¹⁷ where

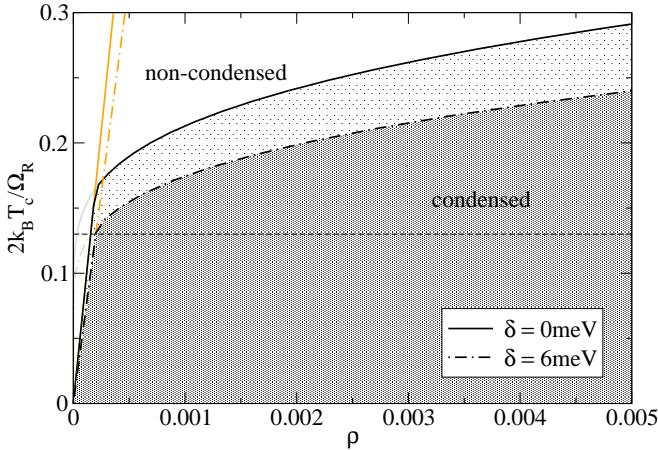


FIG. 6: (Color online) Phase diagram for the dimensionless critical temperature $2k_B T_c / \Omega_R$ versus the dimensionless density ρ for effective zero detuning $\delta = \omega_0 - \varepsilon^* = 0$ meV (ε^* is the energy at which the excitonic optical density has its maximum, and so as seen in Fig. 4, $\delta = 0$ implies $\omega_0 - E_x = -0.94$ meV) (solid black) and for positive detuning $\delta = +6$ meV ($\omega_0 - E_x = +5.06$ meV) (dotted-dashed black) and $\Omega_R = 26$ meV. The mean-field boundaries for the two different detunings are cut-off by the expected linear dependence of the critical temperature, as indicated at extremely low densities [orange (gray) solid and dotted-dashed lines]. The horizontal dashed line marks the temperature of $k_B T = 20$ K which will be used in later figures.

the DoS has been attributed an arbitrary Gaussian-like shape (and moreover where the coupling strength was kept fixed), the density was measured in arbitrary units. Note however that, the fact that the density of states asymptotes to a constant at large densities, and the presence of those exciton states that couple only weakly to light, is responsible only for the asymptotic form of the phase boundary at large densities (well beyond the range shown in Fig. 6 and beyond the validity of our model). At smaller densities, such states have a little effect on the phase boundary. In order to calculate the phase boundary using our numerically calculated distributions, we will solve Eq. (11) and Eq. (12) numerically. How the disorder averaged sums in these equations are to be evaluated has been discussed Sec. II A.

The critical temperature T_c at which the system, for a given density, goes from a non-condensed phase to a condensed phase, is plotted in Fig. 6 for two different values of the detuning $\delta = \omega_0 - \varepsilon^*$, where ε^* is the energy at which the excitonic optical density has its maximum (see Fig. 4). It is clear that increasing the detuning of the cavity mode above the excitonic one decreases the overall photonic fraction and therefore decreases the value of the critical temperature at a given density of excitations. Conversely, if one fixes temperature, the critical density for condensation is higher for larger detuning, as Fig. 6 clearly shows. This dependence is easy to understand in the extremely low density limit, where the

critical temperature varies linearly with density, and is inversely proportional to the polariton mass: By increasing the detuning, the polariton mass also increases.

Having discussed the thermodynamics via the mean-field equations, we now turn in the rest of this paper to the analysis of the optical responses and probes of microcavities, both below and above threshold for condensation, with particular emphasis on the resonant Rayleigh scattering emission. Such optical responses are described by considering fluctuations about the mean-field theory outlined in this section. The spectrum of these fluctuations, and the various optical response functions that these fluctuations describe is the subject of Sec. IV.

As well as describing the optical response, fluctuations about the mean field theory can also be important in describing, in the extremely low density limit, corrections to the mean field thermodynamics. Since the subject of this paper is optical probes, we will not discuss the subject of fluctuation corrections to the critical temperature here, as they have been discussed elsewhere²¹.

For low densities, a bosonic form can be recovered from our Hamiltonian by using the Holstein-Primakoff transformation to express the two-level systems in terms of bosonic operators, and so this low density limit can of course be treated within our model. A smooth crossover between the low density (fluctuation dominated), and the higher density (long-range interaction dominated) regimes can be found by considering fluctuation corrections to the density, as was studied in Ref 21.

IV. OPTICAL PROBES

The optical absorption and emission spectra of a microcavity can be derived by first finding the Green's function describing photon propagation. The non-condensate part of these response functions (i.e. away from zero momentum) may be found in practice by considering the Green's function for fluctuations about the mean-field solution, $\psi_{\mathbf{p},\omega_h} = \psi_{\mathbf{p},0}\delta_{\omega_h,0} + \delta\psi_{\mathbf{p},\omega_h}$, where $\omega_h = 2\pi h/\beta$ is a bosonic Matsubara frequencies, and expanding the action (9) up to quadratic terms:

$$\delta S \simeq \frac{\beta}{2} \sum_{\omega_h, \mathbf{p}, \mathbf{q}} \begin{pmatrix} \delta\psi_{\omega_h, \mathbf{p}}^* \\ \delta\psi_{-\omega_h, -\mathbf{p}} \end{pmatrix}^T \mathcal{G}_{\mathbf{pq}}^{-1}(\omega_h) \begin{pmatrix} \delta\psi_{\omega_h, \mathbf{q}} \\ \delta\psi_{-\omega_h, -\mathbf{q}}^* \end{pmatrix}.$$

This gives the Matsubara inverse photonic Green's function:

$$\mathcal{G}_{\mathbf{pq}}^{-1}(\omega_h) = \begin{pmatrix} K_{\mathbf{pq}}^{(1)}(\omega_h) & K_{\mathbf{pq}}^{(2)}(\omega_h) \\ K_{\mathbf{pq}}^{(2)}(\omega_h) & K_{\mathbf{qp}}^{(1)*}(\omega_h) \end{pmatrix}.$$

Physical response functions can be found by analytic continuation of the imaginary time Matsubara Green's function to real times.⁵⁰ The matrix elements of $\mathcal{G}_{\mathbf{pq}}^{-1}(\omega_h)$ can be expressed in terms of the bare photon energy $\omega_{\mathbf{p}}$ and the excitonic quasi-particle energy E_{α} as follows,

$$K_{\mathbf{pq}}^{(1)}(\omega_h) = \delta_{\mathbf{p},\mathbf{q}}(i\omega_h + \tilde{\omega}_{\mathbf{p}}) + \frac{1}{N} \sum_{\alpha} g_{\alpha,\mathbf{p}}^* g_{\alpha,\mathbf{q}} \frac{\tanh(\beta E_{\alpha})}{E_{\alpha}} \frac{i\omega_h \tilde{\varepsilon}_{\alpha}/2 - E_{\alpha}^2 - (\tilde{\varepsilon}_{\alpha}/2)^2}{\omega_h^2 + 4E_{\alpha}^2} - \delta_{\omega_h,0} \frac{1}{N} \sum_{\alpha} \gamma_{\alpha,\mathbf{p},\mathbf{q}} \quad (14)$$

$$K_{\mathbf{pq}}^{(2)}(\omega_h) = \frac{1}{N} \sum_{\alpha} |g_{\alpha,0}|^2 g_{\alpha,\mathbf{p}}^* g_{\alpha,\mathbf{q}} \frac{\psi^2}{N} \frac{\tanh(\beta E_{\alpha})}{E_{\alpha}} \frac{1}{\omega_h^2 + 4E_{\alpha}^2} - \delta_{\omega_h,0} \frac{1}{N} \sum_{\alpha} \gamma_{\alpha,\mathbf{p},\mathbf{q}} , \quad (15)$$

where

$$\gamma_{\alpha,\mathbf{p},\mathbf{q}} = \beta |g_{\alpha,0}|^2 g_{\alpha,\mathbf{p}}^* g_{\alpha,\mathbf{q}} \frac{\psi^2}{N} \frac{\operatorname{sech}^2(\beta E_{\alpha})}{4E_{\alpha}^2}.$$

It is useful to decompose the photonic Green's function into its momentum diagonal and off-diagonal contributions:

$$K_{\mathbf{pq}}^{(1,2)}(\omega_h) = K_{\mathbf{pp}}^{(1,2)}(\omega_h) \delta_{\mathbf{p},\mathbf{q}} + K_{\mathbf{pq}}^{(1,2)o}(\omega_h) . \quad (16)$$

By treating the off-diagonal terms perturbatively, the translational invariance can be recovered and polariton eigenstates can be labelled by momentum vectors. In the next section, we will focus on the diagonal terms, which characterise both the spectral weight and the photoluminescence emission. Section IV C is then dedicated to RRS, for which we will see that the off-diagonal terms are necessary in order to describe the scattering of an incident photon (via the excitonic component of the microcavity polariton mode) into directions other than its original direction.³⁵

A. Spectral Weight and Photoluminescence

Secondary emission from a semiconductor microcavity after optical excitation is the source of both incoherent PL and coherent RRS. At short times, this emission is dominated by RRS, the coherent scattering from disorder, and so is at the energy of, and coherent with, the incident radiation. At longer times, phonon and particle-particle scattering destroy coherence, and redistribute the energy, leading to a quasi-equilibrium distribution of energies, and thus the incoherent PL emission intensity,

$$P(\omega, \mathbf{p}) = n_B(\omega) W(\omega, \mathbf{p}) , \quad (17)$$

is given by the Bose occupation factor $n_B(\omega)$ times the spectral weight:

$$W(\omega, \mathbf{p}) = 2 \Im \mathcal{G}_{\mathbf{pp}}^{11}(\omega_h) \Big|_{i\omega_h = -\omega - i\eta} . \quad (18)$$

The spectral weight can be interpreted as an absorption coefficient²¹ (the probability to absorb a photon minus the probability to emit a photon), where negative values of $W(\omega, \mathbf{p})$ represent gain. In contrast, the PL $P(\omega, \mathbf{p})$ is always positive.

In calculating the PL, it is convenient to make an approximation by neglecting multiple polariton scattering, while still including the effects of exciton-disorder

scattering to all orders. This is discussed in Ref. 33, where comparison between this approximation and exact numerical calculations show this approximation to be remarkably good. Physically, this is a good limit to consider because the typical exciton-disorder scattering times are very short compared to the inverse frequencies considered in PL. As PL depends on the momentum diagonal part of the photon Green's function, neglect of multiple scattering means in practice averaging over disorder realisations at the level of the inverse photon Green's function, $\mathcal{G}_{\mathbf{pp}}^{-1}(\omega_h)$. Since off-diagonal terms in the inverse Green's function, Eq. (16), break translational invariance, they average to zero, and so scattering between different photon momentum states can thus be neglected. The off-diagonal terms neglected here will however play a crucial role in the case of RRS response, as discussed below.

The spectral weight calculated from this formula, along with the quasi-particle density of states is shown in Fig. 7. We first discuss this in the non-condensed case, where $\psi = 0$, and so $K_{\mathbf{pq}}^{(2)}(\omega_h) = 0$, and the photon's Green function becomes diagonal in particle-hole space, and simplifies to:

$$\mathcal{G}_{\mathbf{pp}}^{-1}(\omega_h) \simeq i\omega_h + \tilde{\omega}_{\mathbf{p}} - \int_{-\infty}^{\infty} d\varepsilon D(\varepsilon) \frac{\tanh(\beta \tilde{\varepsilon}/2)}{i\omega_h + \tilde{\varepsilon}} .$$

This expression describes the coupling of one harmonic oscillator (the photon mode) to many harmonic oscillators (the exciton modes). In the limit of small density, the chemical potential is far below all exciton modes, and so $\tanh(\beta \tilde{\varepsilon}/2) \simeq 1$. In this limit, the result is identical to a bosonic description of excitons sometimes also called the *linear dispersion model*. The underlying fermionic structure appears as a reduction of the effective exciton-photon coupling, due to saturation effects described by the $\tanh(\beta \tilde{\varepsilon}/2)$ term, and discussed in more detail below.

From this *linear dispersion model*, describing one oscillator coupled to many, there are in general two broadened modes at high and low energies – here these are the lower polariton (LP) and upper polariton (UP) – and a continuum of modes associated with the exciton optical density. However, when considering the corresponding spectral weight, modes are weighted by their photonic component, so one primarily sees the LP and UP modes, and only weak emission near the bare excitonic states – the excitonic ‘dark’ states. These three features are clearly visible in Fig. 7, and have been previously predicted by Houdré *et al.*⁵³ making use of a simplified and

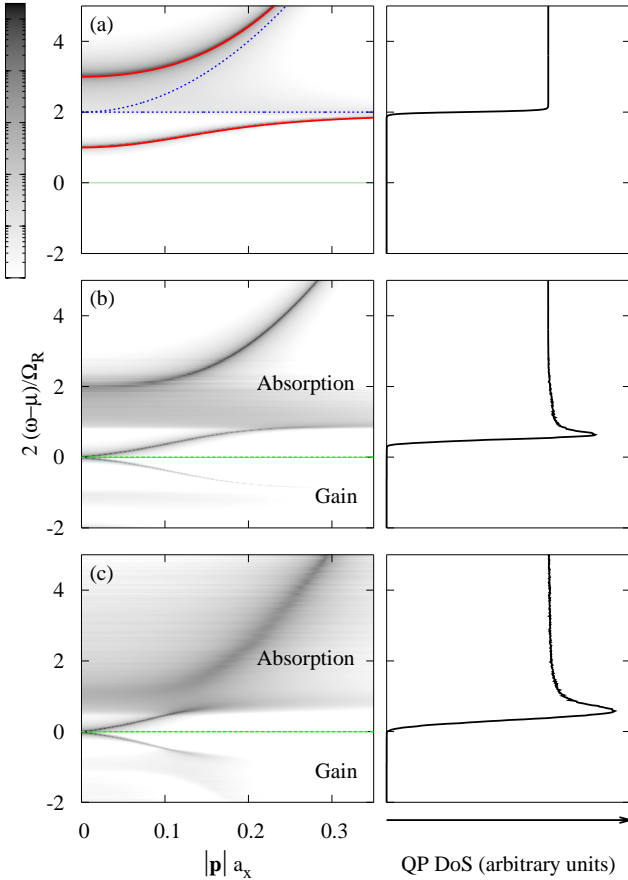


FIG. 7: (Color online) Left column: Contourplot of the spectral weight $W(\omega, \mathbf{p})$ as a function of the dimensionless momentum $|\mathbf{p}|a_x$ and rescaled energy $2(\omega - \mu)/\Omega_R$, for zero detuning $\delta = \omega_0 - \varepsilon^* = 0$ ($\omega_0 - E_x = -0.94$ meV), $\Omega_R = 26$ meV, $k_B T = 20$ K and photon mass $m_{ph}\Omega_R a_x^2/2 = 0.01$. Right column: plot of the quasi-particle DoS for the same choice of parameters as the left column, respectively: (a) non-condensed ($\rho \simeq 0$, $E_x - \mu \simeq 27$ meV) (the bare exciton and photon dispersions [blue (dark gray) dotted line] and the upper and lower polariton dispersions [red (gray) solid line] obtained from the effective coupled oscillator model are shown for comparison); (b) condensed ($\rho \simeq 7.8 \times 10^{-3}$, $E_x - \mu \simeq 11$ meV); (c) condensed ($\rho \simeq 6.7 \times 10^{-2}$, $E_x - \mu \simeq 7$ meV).

exactly solvable model. Note that in the limit of an infinitely narrow spectral width, these dark exciton states become entirely dark, having vanishing photon component. The presence of ‘dark’ exciton states, coexisting with strong coupling polaritons can explain the simultaneous observation of large Rabi splittings and long decay times seen in some experiments.⁵⁴

When the Rabi splitting is substantially larger than the exciton inhomogeneous broadening, (in our case we have $\Omega_R = 26$ meV and the FWHM of the optical density $\sigma^* = 0.94$ meV), there is a substantial difference between broadening of lower and upper polaritons. This is be-

cause the high energy tail of the optical density decays as a power law, while the low energy Lifshitz tail decays exponentially. Thus, the optical density has a larger value at the UP mode than at the LP mode, giving a larger broadening compared to the almost vanishing width of the LP. This description of the polariton linewidth due to the excitonic inhomogeneous broadening coincides with that of Whittaker³³, and it has been well tested experimentally.³⁴

In addition, the location of the LP and UP can be found by making use of an effective two-oscillator model, i.e. assuming a narrow delta-like optical density,

$$D(\varepsilon) \mapsto \left(\frac{\Omega_R}{2} \right)^2 \delta(\varepsilon - \varepsilon^*),$$

where ε^* is the location of the maximum optical density and effectively, the exciton energy. In this case the system reduces to two coupled oscillators, giving unbroadened LP and UP poles at

$$E_{LP,UP} = \frac{\tilde{\omega}_p + \tilde{\varepsilon}^*}{2} \pm \frac{1}{2} \sqrt{(\tilde{\omega}_p - \tilde{\varepsilon}^*)^2 + \overline{\Omega}_R^2}, \quad (19)$$

where, $\overline{\Omega}_R^2 \equiv \Omega_R^2 \tanh(\beta \tilde{\varepsilon}^*/2)$ is the reduced Rabi splitting, due to saturation effects at higher densities. The reduction of $\overline{\Omega}_R$ splitting thus translates directly into a reduction of the LP – UP splitting, and thus a blue-shift of the LP, which at small densities can be shown to be linear. For comparison, the results of this formula are shown by the solid (red) lines in panel (a) of Fig. 7. In Sec. IV B we will discuss the calculation of this linear blue-shift in the low density regime, by evaluating $\overline{\Omega}_R$ as a function of density, making use of the full density of states.

Let us now turn to the signatures of condensation as seen in the spectral weight, and thus in the PL emission (but which are most probably masked in the PL emission by strong emission from the condensate mode). When condensed, the polariton modes are replaced by new collective modes.^{21,25} The lower polariton becomes the linear Goldstone mode, and two branches appear below the chemical potential. The appearance of new excitation branches below the chemical potential is generic to condensation,⁵⁵ however the experiments required to probe these modes are not easy in other Bose condensed systems, such as atomic gases. For this reason, let us briefly discuss the physical origin of these new branches, and the reason they may be observed in optical response of polariton systems. The Bogoliubov spectrum arises because of the possibility of processes that spontaneously either create or destroy two non-condensed particles. (Such processes arise due to scattering from or to the condensate.) As a result of these processes, there is mixing between the propagation of an extra particle, or propagation of a missing particle (i.e. a hole). (Such a language of particle and hole refers to the normal state quasi-particles, in the current case the normal state polaritons.) In the normal state, one can separately calculate the spectral

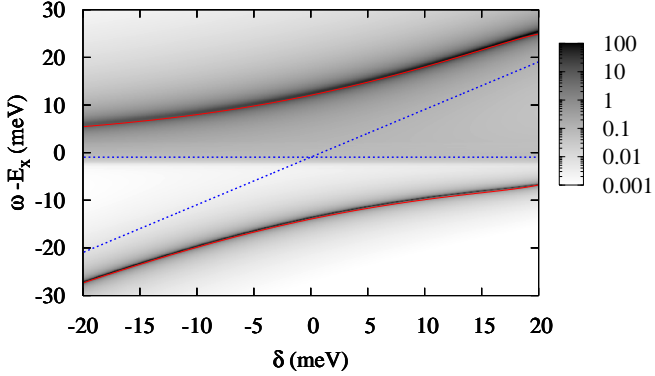


FIG. 8: (Color online) Contourplot of the spectral weight $W(\omega, 0)$ for $\mathbf{p} = 0$ as a function of the detuning $\delta = \omega_0 - \varepsilon^*$ and energy $\omega - E_x$, for a fixed and very low value of density ($\rho \simeq 0$, $E_x - \mu \simeq 27$ meV) and $k_B T = 20$ K ($2k_B T/\Omega_R = 0.13$). The bare exciton and photon dispersions [blue (dark gray) dotted line] and the upper and lower polariton dispersions [red (gray) solid line] obtained from the effective coupled oscillator model are explicitly shown.

weight of particle excitations, which have weight only above the chemical potential, and hole excitations which have weight only below the chemical potential. When condensed, as the ‘particle’ and ‘hole’ spectral weights become mixed, this mixing can lead to spectral weight below the chemical potential that is associated with particle propagation. To observe this weight it is however necessary to have the ability to inject a particle which is not a quasi-particle of the condensed system, i.e. not a Bogoliubov quasiparticle. In atomic experiments this is hard to achieve, but for polaritons can be naturally achieved by injecting a photon. These new branches below the chemical potential are seen as optical gain in the spectral weight (see Fig. 7). Note that the presence of pumping and decay will modify the linear dispersion of the Goldstone mode at low momentum, making it diffusive,²⁶ and that quantisation by disorder may also have some effect.⁵⁶

The spectral weight also contains information about the excitonic quasi-particle DoS of the system. As discussed above for the non-condensed case, this is visible via the appearance of ‘dark’ exciton states [see Figs. 8 and 7(a)]. When condensed, there is a coherent field that modifies the energies of these excitonic quasi-particle states, as given in Eq. (13), and thus modifies their density of states. The density of states given by taking the energy of such modes is shown by the right column of Fig. 7, and can be compared to the corresponding faint features seen in the photon spectral weight in the left column.

The change to the quasi-particle density of states that occurs on condensation requires some explanation. As mentioned earlier, the change of this spectrum is similar to that seen in the BCS theory of superconductivity,

as such it is surprising that there is no gap in the density of states of Fig. 7. In fact, there would be a gap if the distribution of oscillator strengths were replaced with the mean square oscillator strength. In that case, there would be a branch cut, and a $(E - g\psi/\sqrt{N})^{-1/2}$ singularity in the density of states. However, with the full distribution of oscillator strengths, one finds that there is always a non-vanishing probability of arbitrarily small oscillator strengths. (Note that if the oscillator strength were zero, the corresponding state would not contribute to any photon response, but for an arbitrarily small coupling, it has some contribution.) Thus, the contribution of these weakly coupled exciton states in effect smoothes out the gap. Thus, this system can be vaguely described as ‘gapless fermion condensation’, analogous to ‘gapless superconductivity’, but through a mechanism very different to the standard Abrikosov-Gor’kov mechanism considered in superconductors.^{18,50}

As one moves away from the chemical potential, the mixing of ‘particle’ and ‘hole’ modes described by the Bogoliubov spectrum reduces. As a result, far above the chemical potential, the modes are much as the uncondensed case, and the far below the chemical potential, the new modes disappear. To explain this quantitatively, it is clearer to discuss the case of weakly interacting Bose gas.⁵⁵ Writing the Bogoliubov mode energy as $\xi_{\mathbf{p}} = \sqrt{\epsilon_{\mathbf{p}}(\epsilon_{\mathbf{p}} + 2\mu)}$, where $\mu = g\psi^2$ is the mean-field value, the spectral weight is given by:

$$W(\omega, \mathbf{p}) = \frac{\epsilon_{\mathbf{p}} + \mu + \xi_{\mathbf{p}}}{2\xi_{\mathbf{p}}} \delta(\omega - \xi_{\mathbf{p}}) - \frac{\epsilon_{\mathbf{p}} + \mu - \xi_{\mathbf{p}}}{2\xi_{\mathbf{p}}} \delta(\omega + \xi_{\mathbf{p}}),$$

It is thus clear that at large momenta, where $\xi_{\mathbf{p}} \simeq \epsilon_{\mathbf{p}} + \mu$, the coefficient of the first delta function (modes above the chemical potential) will go to one, and the the coefficient of the second (modes below) will be suppressed to zero (roughly quadratically in energy).

In contrast to the power law suppression of the spectral weight of modes far below the chemical potential, the PL signal from modes far above zero is suppressed exponentially by the thermal occupation of these modes [see Eq. (17)], while below the chemical potential, there is no such decay. However, this discussion neglects emission from the condensate mode, which should included at zero momentum, as defined in Eq. (17). To see a noticeable change of the normal modes requires a relatively large condensate density. Due to instrumental broadening, the presence of emission from this large condensate density might obscure emission from the normal modes, so they may only be weakly visible, as shown in Fig. 9. As discussed below, RRS may provide a means of escape from this problem.

B. Lower Polariton Blue-Shift

Before discussing the RRS response, let us briefly discuss a point mentioned above – the calculation of the LP blue-shift as a function of density, making use of the full

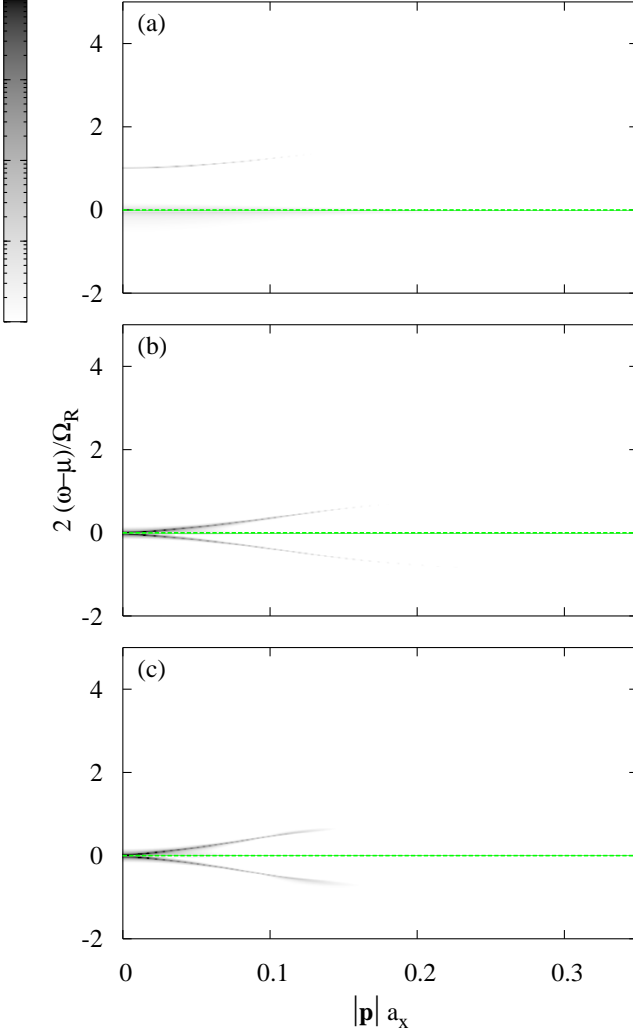


FIG. 9: (Color online) Contourplot of the incoherent PL $P(\omega, \mathbf{p})$ as a function of the dimensionless momentum $|\mathbf{p}|a_x$ and rescaled energy $2(\omega - \mu)/\Omega_R$, for detuning $\omega_0 - E_x = -0.94\text{meV}$, $\Omega_R = 26\text{meV}$, $k_B T = 20\text{K}$ and $m_{\text{ph}}\Omega_R a_x^2/2 = 0.01$: (a) non-condensed ($\rho \simeq 0$, $E_x - \mu \simeq 27\text{meV}$); (b) condensed ($\rho \simeq 7.8 \times 10^{-3}$, $E_x - \mu \simeq 11\text{meV}$); (c) condensed ($\rho \simeq 6.7 \times 10^{-2}$, $E_x - \mu \simeq 7\text{meV}$).

density of states, and our model of saturation effects (7). This can be observed in PL experiments by the change of blue-shift as a function of intensity of the non-resonant pumping.

In the non condensed regime, the blue-shift of the LP in our model is a consequence of the saturation of the (disordered) energy levels. Following the narrow band-width limit described in Eq. (19), this saturation blue-shift can be found if one has an expression for the chemical potential at a given temperature and density. In the low density limit, the expression for density ρ as a function of μ [Eq. (12) with $\psi = 0$] can be inverted in terms of elementary functions. As illustrated by Fig. 5, in the low density limit, the chemical potential is far below the

band edge. Thus, there are two significant contributions to density: one from low energies, in the tail of the DoS, but at large occupation, and one from high energies, in the tail of the occupation, but at large DoS, thus:

$$\rho \simeq \int_{-\infty}^{\mu} \frac{d\varepsilon}{\mathcal{R}_{\text{y}_x}} e^{-2|\varepsilon|/W_\rho} + \int_0^{\infty} \frac{d\varepsilon}{\mathcal{R}_{\text{y}_x}} e^{-(\varepsilon - \mu)/k_B T}. \quad (20)$$

Here $W_\rho/2 = 0.32\text{meV}$ is the energy which characterises the exponential decay of DoS in the tail of the Lifshitz states – this coefficient is extracted by an exponential fit to our numerical DoS. At a temperature of $k_B T = 20\text{K} = 1.72\text{meV}$, the dominant contribution to the density is given by the second integral and the chemical potential increases logarithmically with the density:

$$\rho \simeq \frac{k_B T}{\mathcal{R}_{\text{y}_x}} e^{\mu/k_B T}. \quad (21)$$

From this expression, and from the coupled oscillator expressions of the LP Eq. (19), we can explicitly derive the reduced Rabi splitting due to saturation effects,

$$\overline{\Omega}_R \simeq \Omega_R \left(1 - 2e^{-\varepsilon^*/k_B T} \frac{\mathcal{R}_{\text{y}_x}}{k_B T} \rho \right)^{1/2}$$

and the LP blue-shift, which is thus linear in this low-density regime:

$$\delta E_{\text{LP}} \equiv E_{\text{LP}}(\rho) - E_{\text{LP}}(0) \sim \Omega_R n \frac{1}{m_x k_B T}, \quad (22)$$

where we have reintroduced here the density n per unit volume. Remaining at small densities, but now considering the low temperature limit, $W_\rho/2 > k_B T$, then the dominant term in Eq. (20) is the first, and so Eq. (22) should be modified by replacing the thermal length $(m_x k_B T)^{-1}$, by a characteristic disorder length $(m_x W_\rho)^{-1}$.

It is instructive to compare this result with that for a clean system; in this case blue-shift of the LP has been attributed either due to Coulomb interaction⁴⁶ or to saturation effects⁴⁷ (where the expression given here is valid only in the dilute limit):

$$\begin{aligned} \delta E_{\text{Coul}}^0 &\sim \mathcal{R}_{\text{y}_x} n a_x^2 \\ \delta E_{\text{sat}}^0 &\sim \Omega_R n a_x^2. \end{aligned}$$

Because the excitonic Rydberg \mathcal{R}_{y_x} can be of the same order of magnitude as the Rabi splitting Ω_R , in a clean system the two shifts can be expected to be of the same order of magnitude. Considering just saturation effects, the difference between clean and dirty systems is that, at low temperature, in a clean system blue-shift depends on exciton number per square Bohr radius, while in a disordered system the relevant length is that characteristic of the disorder potential, which is in general larger than the Bohr radius. Finally, we wish to observe that there is a distinction between Coulomb and saturation effects: Coulomb interactions result in a blue-shift of both

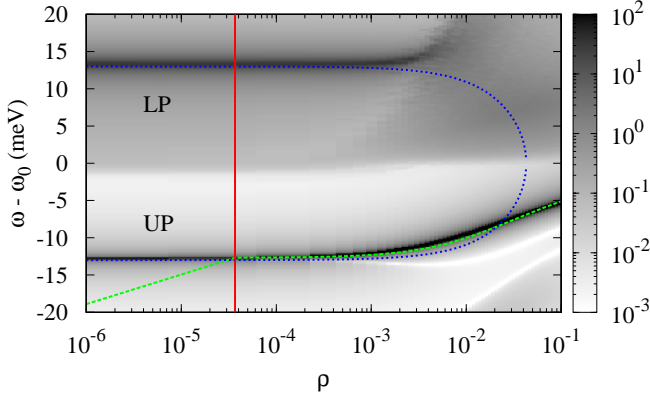


FIG. 10: (Color online) Contourplot of the spectral weight $W(\omega, 0)$ for $\mathbf{p} = 0$ as a function of the dimensionless density ρ and the rescaled energy $\omega - \omega_0$, for zero detuning ($\omega_0 - E_x = -0.94$ meV) and $k_B T = 20$ K ($2k_B T/\Omega_R = 0.13$). The rescaled chemical potential $(\mu - \omega_0)$ [green (light gray) dashed], the non-condensed lower and upper polariton modes from the two coupled oscillator model [blue (dark gray) dotted], and the critical density for condensation $\rho_c \simeq 3.7 \times 10^{-5}$ [vertical solid red (dark gray) line] are shown for comparison.

the LP and UP, while saturation leads to a blue-shift of the LP and a red shift of the UP, i.e. a collapse of the Rabi splitting. Thus, these effects can be experimentally distinguished, and their relative magnitudes determined.

In the condensed regime, the equivalent of the LP is the Goldstone linear mode, which by definition starts at the chemical potential. Thus, the observed blue-shift is a direct observation of chemical potential vs. density. Figure 10 shows the variation of the spectral weight at zero momentum as a function of density, from which the energy of the zero momentum LP and UP modes can be extracted. Also shown, for comparison, is the chemical potential vs. density (dashed green line). The locking of the LP mode to the chemical potential beyond the critical density (red solid line) is clearly visible, and the behaviour of the LP mode vs density allows the extraction of density from an experimental measurement of LP blue-shift.

C. Resonant Rayleigh Scattering

As described in Refs. 35,36, the RRS intensity describes the probability to inject a photon into the cavity with momentum \mathbf{p} , and detect a coherent photon at \mathbf{q} with $\mathbf{p} \neq \mathbf{q}$. The intensity of such a signal may be written as:

$$I_{\mathbf{pq}}(\omega) = |\mathcal{G}_{\mathbf{pq}}^{11}|^2|_{i\omega_h = -\omega - i\eta}. \quad (23)$$

Since this involves the off-diagonal momentum space components of the Green's function, it is necessary to include the off-diagonal momentum components of the

inverse Green's function Eq. (16). However, as discussed in Sec. IV, we will consider only a single polariton scattering and again neglect multiple polariton scattering (but include all orders of exciton-disorder scattering). Such an approximation is reasonable for the same reasons discussed at the start of Sec. IV.

In the following, we propose using the RRS signal to probe the excitation spectrum in the presence of a polariton condensate. It is therefore necessary to be able to separate the RRS signal from the strong photoluminescence that would arise from the equilibrium state with large polariton density. Further, since a condensed polariton system may have a strong nonlinear response to an applied probe (i.e. stimulated scattering if the probe significantly affects the population of polariton modes), it is necessary to use a weak RRS probe. Fortunately, the coherent nature of RRS allows exactly this: one can detect a weak RRS signal by phase sensitive measurement, as is discussed in detail in Appendix A. Hence, the limit on intensity of the probe is provided by the sensitivity of the CCD camera, and not by the incoherent photoluminescence background. This therefore allows a probe sufficiently weak that only the linear RRS response is seen, and nonlinear effects can be avoided.

When non-condensed, the single polariton scattering expansion of the photon Green's function in the off-diagonal terms gives

$$I_{\mathbf{pq}}(\omega_h) \simeq \frac{1}{|K_{\mathbf{pp}}^{(1)}(\omega_h)|^2} |K_{\mathbf{pq}}^{(1)o}(\omega_h)|^2 \frac{1}{|K_{\mathbf{qq}}^{(1)}(\omega_h)|^2}. \quad (24)$$

The factors $|K_{\mathbf{qq}}^{(1)}(\omega_h)|^{-2}$ appearing here can be interpreted as a filter, allowing a response only when the outgoing (or equivalently incoming for $\mathbf{q} \rightarrow \mathbf{p}$) momentum has an energy close to the polariton mode at the given energy. This means that $|\mathbf{p}| \simeq |\mathbf{q}|$ and so is responsible for the ring-shaped RRS signal observed in experiments.^{37,38} In contrast, the term $|K_{\mathbf{p},\mathbf{q}}^{(1o)}(\omega_h)|^2$ describes scattering between momentum states via polariton-exciton-polariton scattering. This term has a large variation from disorder realization to disorder realization, and is the reason for the speckle seen in RRS experiments. This speckle, and the disorder averaged RRS intensity are shown for comparison in Fig. 11. As the precise speckle pattern depends on the precise disorder realization, the most we can reasonably do is to describe the statistical properties of this speckle, thus the disorder averaged RRS signal shown in Fig. 1 would in experiment represent the envelope of the RRS speckle pattern.

When condensed, the expression for the RRS intensity becomes more complicated, but can still be written in the form of a filter and scattering part:

$$I_{\mathbf{pq}}(\omega) \simeq F_{\mathbf{p}} S_{\mathbf{pq}} F_{\mathbf{q}}, \quad (25)$$

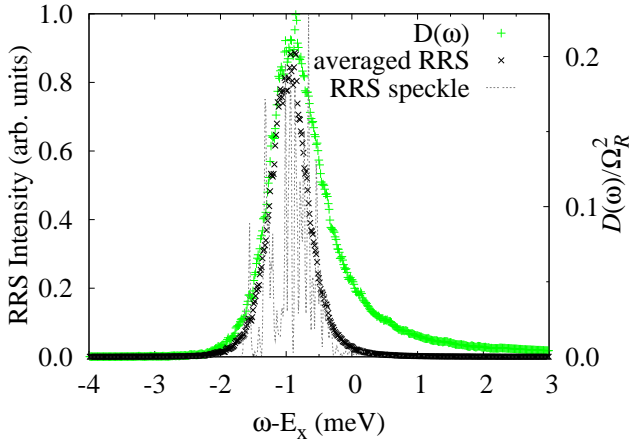


FIG. 11: (Color online) Excitonic speckle pattern $|K_{\mathbf{p},\mathbf{q}}^{(1o)}(\omega_h)|^2|_{i\omega_h=-\omega-i\eta}$ for a single disorder realization (gray dotted line) and its disorder average (black cross symbols) versus energy for $|\mathbf{p}| = |\mathbf{q}| = 36^\circ$ and a 90° azimuthal angle, $\mathbf{p} = (0, 6.3 \times 10^4) \text{ cm}^{-1}$ and $\mathbf{q} = (6.3 \times 10^4, 0) \text{ cm}^{-1}$. For comparison, we also plot the excitonic optical density [green (light gray) plus symbols].

where the filter and scattering terms are respectively:

$$F_{\mathbf{p}} = \left| |K_{\mathbf{p}\mathbf{p}}^{(1)}|^2 - (K_{\mathbf{p}\mathbf{p}}^{(2)})^2 \right|^{-2},$$

$$S_{\mathbf{p}\mathbf{q}} = \left| K_{\mathbf{p}\mathbf{q}}^{(1)o} K_{\mathbf{p}\mathbf{p}}^{(1)*} K_{\mathbf{q}\mathbf{q}}^{(1)*} + K_{\mathbf{q}\mathbf{p}}^{(1)o*} K_{\mathbf{p}\mathbf{p}}^{(2)} K_{\mathbf{q}\mathbf{q}}^{(2)} \right. \\ \left. - K_{\mathbf{p}\mathbf{q}}^{(2)o} \left(K_{\mathbf{p}\mathbf{p}}^{(2)} K_{\mathbf{q}\mathbf{q}}^{(1)*} + K_{\mathbf{p}\mathbf{p}}^{(1)*} K_{\mathbf{q}\mathbf{q}}^{(2)} \right) \right|^2. \quad (26)$$

As in the non-condensed case, the filter function $F_{\mathbf{p}}$ restricts the allowed incoming and outgoing momenta to those for which the normal modes have the injected energy. However, as discussed earlier, in the presence of a condensate, the normal modes supported are no longer the LP and UP, but instead the new Bogoliubov-like quasi-modes.

The decay of spectral weight associated with modes far below the chemical potential, as discussed in Sec. IV A still applies (this can clearly be seen in Fig. 1, Fig. 7 and Fig. 9). However, since the energy of the RRS signal is controlled by the energy of the incident photon, it is possible to study modes far above the chemical potential, which would have negligible equilibrium occupation, and thus negligible weight in the PL signal. Both for this reason, and because of the ability to discriminate between the coherent RRS signal and incoherent photoluminescence, RRS provides a very powerful tool to study the interesting properties of condensed polariton systems.

V. CONCLUSIONS

In this paper we have analysed and compared different optical responses of a condensate of microcavity po-

laritons. One of the conclusions of this work is that, compared to photoluminescence studies, the energy and momentum resolved resonant Rayleigh scattering spectra provides many advantages in probing a condensed phase and in studying the associated coherent excitation spectrum. In particular, resonant Rayleigh scattering, by collecting the signal at a different angle from that at which the system is probed, allows one to look directly at characteristic features of the condensed phase excitation spectrum. Such features, like the Goldstone modes both above and below the chemical potential, are weak in photoluminescence emission and are likely to be masked by the strong emission from the condensate in the lowest momentum state. In contrast, Rayleigh scattering, being coherent with the probe, can be distinguished from condensate emission.

One can ask why the accurate description of excitonic disorder considered in this paper is necessary, when the microcavity photon introduces a long length scale which averages over disorder. One might also compare this system with other excitonic systems, such as double quantum wells,⁵⁷ where high density of dipole-dipole interacting excitons quickly screens the disorder.^{58,59} The answer to this question is that the large ratio of exciton to photon mass means firstly that exciton density required for condensation in microcavities is far less than in double quantum wells; and secondly that those exciton states involved in forming the thermally occupied polariton modes are strongly localised exciton states (i.e. influenced by disorder beyond Born approximation). One of the consequences of an accurate treatment of disorder in microcavities is that the blue-shift of the lower polaritons due to saturation effects depends on a length scale characteristic of disorder and temperature, which can be much larger than the Bohr radius, this length playing an equivalent role in the clean system. This effect can be important in determining the polariton densities from the measured blue-shift in current experiments.

An important consequence of disorder is that the exciton-light coupling strength is characterised by a full distribution. In the non-condensed phase, the optical density alone determines the photoluminescence response, while for resonant Rayleigh scattering the averaged fourth power of the oscillator strength is required. However, in the condensed phase one has to consider the entire distribution for each exciton energy. For energies close to and above the band edge, there is always a non-vanishing probability of an arbitrarily small oscillator strength. For this reason, in contrast to examples like BCS superconductivity, one can show that the quasi-particle spectrum does not have a hard gap.

In conclusion, we have considered how an accurate treatment of disorder on the single-particle excitonic level, when elevated to the many body problem of interacting microcavity polaritons, leads to a variety of interesting features in various optical responses and probes of the condensed phase.

Acknowledgments

We are grateful to Roland Zimmermann, Wolfgang Langbein and Ben Simons for suggestions and useful discussions. F.M.M. and M.H.S. would like to acknowledge financial support from EPSRC. J.K. would like to acknowledge financial support from the Lindemann Trust. This work is supported by the EU Network “Photon mediated phenomena in semiconductor nanostructures” HPRN-CT-2002-00298.

APPENDIX A: PHASE SENSITIVE DETECTION OF RESONANT RAYLEIGH SIGNAL

In this appendix we show how the coherent nature of the resonant Rayleigh signal allows a weak coherent probe to be detected in the presence of strong incoherent photoluminescence. The Rayleigh scattering probe is a perturbation, $\hat{H} = \hat{H}_0 + \hat{V}$, which in the rotating wave approximation may be written as:

$$\hat{V} = A_0 \left(\hat{\psi}_{\mathbf{p}}^\dagger e^{i\Omega t} + \hat{\psi}_{\mathbf{p}} e^{-i\Omega t} \right). \quad (\text{A1})$$

This describes a probe at wavevector \mathbf{p} , frequency Ω , of strength A_0 . The RRS signal is the coherent scattering of this probe to other wavevectors. To isolate the part of the emission that is coherent with the probe, one may use a homodyne measurement, interfering the emission with part of the probe signal. This corresponds to measuring the spectrally resolved emission intensity :

$$P(\omega, \mathbf{q}) = \int dt e^{i\omega t} P(t, \mathbf{q}), \quad (\text{A2})$$

where

$$P(t, \mathbf{q}) = \sum_n e^{\beta(F-E_n)} \times \langle n | \left[\hat{\psi}_{\mathbf{q}}^\dagger(t) + A_1 e^{-i(\Omega t+\phi)} \right] \left[\hat{\psi}_{\mathbf{q}}(0) + A_1 e^{i\phi} \right] | n \rangle,$$

and where A_1 is the strength of the homodyne mixing, and ϕ is a phase delay introduced between the probe and the homodyne signal. The states $|n\rangle$ are the eigenstates of the system without the probe, given by $\hat{H}_0|n\rangle = E_n|n\rangle$; F is the free energy, for normalization.

The principle of phase sensitive detection is to vary the phase delay, and to extract the part of $P(\omega, \mathbf{q})$ which depends on this phase delay. Since the background PL does not depend on the phase delay, this allows one to separate a small but phase dependent signal from a strong but phase independent background.

The part of the signal that depends on phase is:

$$P_\phi(t, \mathbf{q}) = A_1 \sum_n e^{\beta(F-E_n)} \times \left[\langle n | \hat{\psi}_{\mathbf{q}}^\dagger(t) | n \rangle e^{i\phi} + \langle n | \hat{\psi}_{\mathbf{q}}(0) | n \rangle e^{-i(\phi+\Omega t)} \right]. \quad (\text{A3})$$

Standard first order time-dependent perturbation theory, using the perturbation in Eq. (A1) yields:

$$\langle n | \hat{\psi}_{\mathbf{q}}^\dagger(t) | n \rangle = A_0 \sum_m \left[\frac{\langle n | \hat{\psi}_{\mathbf{q}}^\dagger | m \rangle \langle m | \hat{\psi}_{\mathbf{p}} | n \rangle}{E_n - E_m - \Omega - i\eta} \right. \\ \left. - \frac{\langle n | \hat{\psi}_{\mathbf{p}} | m \rangle \langle m | \hat{\psi}_{\mathbf{q}}^\dagger | n \rangle}{E_m - E_n - \Omega - i\eta} \right] e^{-i\Omega t} + [\dots] e^{i\Omega t}. \quad (\text{A4})$$

The term written $[\dots]$ is similar to the first term, but with $\Omega \mapsto -\Omega$ and $\psi_{\mathbf{p}} \mapsto \psi_{\mathbf{p}}^\dagger$. Inserting this signal into Eq. (A3) and then into Eq. (A2), it can be seen that such a term gives a signal at frequency $\omega = -\Omega$, and so can be clearly separated and ignored. Inserting the first term into Eq. (A3), one can write:

$$\sum_n e^{\beta(F-E_n)} \langle n | \hat{\psi}_{\mathbf{q}}^\dagger(t) | n \rangle = \sum_{n,m} e^{\beta(F-E_n)} \times \left[1 - e^{\beta(E_n-E_m)} \right] \frac{\langle n | \hat{\psi}_{\mathbf{q}}^\dagger | m \rangle \langle m | \hat{\psi}_{\mathbf{p}} | n \rangle}{E_n - E_m - \Omega - i\eta}, \quad (\text{A5})$$

which is the definition of the retarded Green's function,⁵⁰ $G_{R,\mathbf{pq}}^{11}(\Omega) = \mathcal{G}_{\mathbf{pq}}^{11}|_{i\omega_h=-\Omega-i\eta}$. By repeating the same analysis for the second term in Eq. (A3), one can then write:

$$P_\phi(t, \mathbf{q}) = 2A_1 A_0 |G_{R,\mathbf{pq}}^{11}(\Omega)| \cos(\phi + \phi_0) e^{-i\Omega t}, \quad (\text{A6})$$

where ϕ_0 is the phase of the retarded Green's function. Hence, the phase-dependent part of the luminescence is given by the off-diagonal in momentum space part of the retarded Green's function, i.e. the RRS signal.

^{*} Present address: Rudolf Peierls Centre for Theoretical Physics, 1 Keble Road, Oxford OX1 3NP, UK

[†] Present address: Cavendish Laboratory, University of Cambridge, Madingley Road, Cambridge CB3 0HE, UK

¹ L. V. Keldysh and Yu. V. Kopaev, *Fiz. Tverd. Tela (Leningrad)* **6**, 2791 (1964) [Sov. Phys. Solid State **6**, 2219 (1965)].

² J. J. Hopfield, *Phys. Rev.* **112**, 1555 (1958).

³ C. Weisbuch, M. Nishioka, A. Ishikawa, and Y. Arakawa, *Phys. Rev. Lett.* **69**, 3314 (1992).

⁴ Le Si Dang, D. Heger, R. André, F. Boeuf, and R. Romestain, *Phys. Rev. Lett.* **81**, 3920 (1998).

⁵ P. Senellart and J. Bloch, *Phys. Rev. Lett.* **82**, 1233 (1999).

⁶ Y. Yamamoto, *Nature* **405**, 629 (2000)

⁷ P. G. Savvidis, J. J. Baumberg, R. M. Stevenson, M. S. Skolnick, D. M. Whittaker, and J. S. Roberts, *Phys. Rev.*

Lett. **84**, 1547 (2000)

⁸ M. Saba, C. Ciuti, J. Bloch, V. Thierry-Mieg, R. André, Le Si Dang, S. Kundermann, A. Mura, G. Bongiovanni, J. L. Staehli, B. Deveaud, *Nature* **414**, 731 (2001).

⁹ H. Deng, G. Weihs, C. Santori, J. Bloch, and Y. Yamamoto, *Science* **298**, 199 (2002); H. Deng, G. Weihs, D. Sone, J. Bloch, and Y. Yamamoto, *PNAS* **100**, 15318 (2003).

¹⁰ G. Weihs, H. Deng, D. Sone, and Y. Yamamoto, *Physica Status Solidi A*, **201**, 625 (2004).

¹¹ M. Richard, J. Kasprzak, R. Romestain, R. André, and Le Si Dang, *Phys. Rev. Lett.* **94**, 187401 (2005).

¹² M. Richard, J. Kasprzak, R. André, R. Romestain, L. S. Dang, G. Malpuech, and A. Kavokin, *Phys. Rev. B* **72**, 201301 (2005).

¹³ H. Deng, D. Press, S. Gotzinger, G. S. Solomon, R. Hey, K. H. Ploog, Y. Yamamoto, *Phys. Rev. Lett.* **97**, 146402 (2006).

¹⁴ J. Kasprzak, M. Richard, S. Kundermann, A. Baas, P. Jeanbrun, J. Keeling, F. M. Marchetti, M. H. Szymanska, R. André, J. L. Staehli, V. Savona, P. B. Littlewood, B. Devaud, and Le Si Dang, *Nature*, **443**, 409 (2006).

¹⁵ F. Tassone, C. Piermarocchi, V. Savona, A. Quattropani, and P. Schwendimann, *Phys. Rev. B* **56**, 7554 (1997); F. Tassone and Y. Yamamoto, *Phys. Rev. B* **59**, 10830 (1999).

¹⁶ A. I. Tartakovskii, M. Emam-Ismail, R. M. Stevenson, M. S. Skolnick, V. N. Astratov, D. M. Whittaker, J. J. Baumberg, and J. S. Roberts, *Phys. Rev. B* **62**, R2283 (2000).

¹⁷ P. R. Eastham and P. B. Littlewood, *Solid State Commun.* **116**, 357 (2000); *Phys. Rev. B* **64**, 235101 (2001).

¹⁸ M. H. Szymanska and P. B. Littlewood, *Solid State Commun.* **124**, 103 (2002); M. H. Szymanska, P. B. Littlewood, and B. D. Simons, *Phys. Rev. A* **68**, 013818 (2003).

¹⁹ A. Kavokin and G. Malpuech, *Cavity polaritons*, in *Thin Films and Nanostructures* vol. 32 (Elsevier, NY, 2003).

²⁰ F. P. Laussy, G. Malpuech, A. Kavokin, and P. Begenwald, *Phys. Rev. Lett.* **93**, 016402 (2004); A. Kavokin, G. Malpuech, and F. P. Laussy, *Phys. Lett. A* **306**, 187 (2003).

²¹ J. Keeling, P. R. Eastham, M. H. Szymanska, P. B. Littlewood, *Phys. Rev. Lett.* **93**, 226403 (2004); *Phys. Rev. B* **72**, 115320 (2005).

²² F. M. Marchetti, B. D. Simons, and P. B. Littlewood, *Phys. Rev. B* **70**, 155327 (2004); F. M. Marchetti, M. H. Szymanska, P. R. Eastham, B. D. Simons, and P. B. Littlewood, *Solid State Commun.* **134**, 111 (2005).

²³ T. D. Doan, Huy Thien Cao, D. B. Tran Thoai, and H. Haug, *Phys. Rev. B* **72**, 085301 (2005).

²⁴ I. Shelykh, F.P. Laussy, A. V. Kavokin, and G. Malpuech, preprint cond-mat/0503402.

²⁵ F. M. Marchetti, J. Keeling, M. H. Szymanska, and P. B. Littlewood, *Phys. Rev. Lett.* **96**, 066405 (2006).

²⁶ M. H. Szymanska, J. Keeling and P. B. Littlewood, *Phys. Rev. Lett.* **96**, 230602 (2006).

²⁷ D. Porras and C. Tejedor, *Phys. Rev. B* **67**, 161310(R) (2003).

²⁸ D. Sarchi and V. Savona, *AIP Conf. Proc.* **893**, 401 (2007).

²⁹ P. Schwendimann and A. Quattropani, *Phys. Rev. B* **74**, 045324 (2006).

³⁰ R. Zimmermann, F. Grosse, and E. Runge, *Pure and Appl. Chem.* **69**, 1179 (1997); R. Zimmermann and E. Runge, *Phys. Stat. Sol. (a)* **164**, 511 (1997).

³¹ E. Runge and R. Zimmermann, in *Advances in Solid State Physics*, vol. **38** (Ed. B. Kramer), Vieweg, Braunschweig (1998); E. Runge and R. Zimmermann, *Phys. Stat. Sol.* (b) **221**, 269 (2000).

³² E. Runge, "Excitons in Semiconductors Nanostructures", in *Solid State Physics* vol. **57**, Academic Press, Amsterdam (2002).

³³ D. M. Whittaker, *Phys. Rev. Lett.* **80**, 4791 (1998).

³⁴ P. Borri, W. Langbein, U. Woggon, J. R. Jensen, and J. M. Hvam *Phys. Rev. B* **63**, 035307 (2001).

³⁵ D. M. Whittaker, *Phys. Rev. B* **61**, R2433 (2000).

³⁶ A. V. Shchegrov, J. Bloch, D. Birkedal, and J. Shah, *Phys. Rev. Lett.* **84**, 3478 (2000).

³⁷ T. Freixenet, B. Sermage, J. Bloch, J. Y. Marzin, and R. Planel, *Phys. Rev. B* **60**, R8509 (1999).

³⁸ W. Langbein and J. M. Hvam, *Phys. Rev. Lett.* **88**, 047401 (2002).

³⁹ I. Carusotto and C. Ciuti, *Phys. Rev. Lett.* **93**, 166401 (2004); C. Ciuti and I. Carusotto, *Phys. Status Solidi B* **242**, 2224 (2005).

⁴⁰ S. D. Baranovskii and A. L. Éfros, *Fiz. Tekh. Poluprovodn.* **12**, 2233 (1978) [Sov. Phys. Semicond. **12**, 1328 (1979)].

⁴¹ N. N. Ablyazov, M. É. Raikh, and A. L. Éfros, *Fiz. Tverd. Tela (Leningrad)* **25**, 353 (1983) [Sov. Phys. Solid State **25**, 199 (1983)].

⁴² M. Litinskaya, G. C. La Rocca, and V. M. Agranovich, *Phys. Rev. B* **64**, 165316 (2001).

⁴³ R. Zimmerman, E. Runge, and V. Savona, "Theory of resonant secondary emission: Rayleigh scattering versus luminescence", in *Quantum coherence, correlation and decoherence in semiconductor nanostructures* (Ed. T. Taka-gahar), Elsevier Science (2003).

⁴⁴ I. M. Lifshitz, *Adv. Phys.* **13**, 483 (1964); J. Zittartz and J. S. Langer, *Phys. Rev.* **148**, 741 (1966); B. I. Halperin and M. Lax, *Phys. Rev.* **148**, 722 (1966).

⁴⁵ M. C. Payne, M. P. Teter, D. C. Allan, T. A. Arias and J. D. Joanopoulos, *Rev. Mod. Phys.* **62**, 1045 (1992).

⁴⁶ G. Rochat, C. Ciuti, V. Savona, C. Piermarocchi, A. Quattropani, and P. Schwendimann, *Phys. Rev. B* **61**, 13856 (2000).

⁴⁷ C. Ciuti P. Schwendimann, B. Deveaud, and A. Quattropani, *Phys. Rev. B* **62**, R4825 (2000).

⁴⁸ V. N. Popov and S. A. Fedotov, *Zh. Eksp. Teor. Fiz.* **94**, 183 (1988) [Sov. Phys. JETP **67**, 535 (1988)].

⁴⁹ M. Gurioli, F. Bogani, L. Cavigli, H. Gibbs, G. Khitrova, and D. S. Wiersma, *Phys. Rev. Lett.* **94**, 183901 (2005).

⁵⁰ A. A. Abrikosov, L. P. Gor'kov and I. E. Dzyaloshinski *Methods of Quantum Field Theory in Statistical Physics*. (Dover, New York) 1975.

⁵¹ M. Holland, S.J.J.M.F. Kokkelmans, M.L. Chiofalo, and R. Walser, *Phys. Rev. Lett.* **87**, 120406 (2001); E. Timmermans, K. Furuya, P.W. Milonni, and A.K. Kerman, *Phys. Lett. A* **285**, 228 (2001); Y. Ohashi, A. Griffin, *Phys. Rev. Lett.* **89**, 130402 (2002).

⁵² P. B. Littlewood, P. R. Eastham, J. M. J. Keeling, F. M. Marchetti, B. D. Simons, M. H. Szymanska, *J. Phys.: Condens. Matter* **16** S3597 (2004).

⁵³ R. Houdré, R. P. Stanley, and M. Illegems, *Phys. Rev. A* **53**, 2711 (1996).

⁵⁴ A. V. Mintsev, L. V. Butov, C. Ell, S. Mosor, G. Khitrova and H. M. Gibbs, *Pis'ma Zh. Eksp. Teor. Fiz.* **76**, 742 (2002) [Sov. Phys. JET Lett. **76**, 637 (2002)]

⁵⁵ L. P. Pitaevskii and S. Stringari, *Bose Einstein Condensation* (Clarendon Press, Oxford, 2003).

⁵⁶ A. V. Kavokin. Private Communication.

⁵⁷ L. V. Butov, *J. Phys.: Condens. Matter* **16** R1577 (2004).

⁵⁸ A. L. Ivanov, *Europhys. Lett.* **59**, 586 (2002).
⁵⁹ R. Zimmermann, *Solid State Comm.* **134**, 43 (2005).
⁶⁰ Formally this can be seen by representing the two levels as

a spin 1/2, and making a Holstein-Primakoff transformation of our model.